SOME THEORETICAL THINKING ON THE CHANGING TROPICAL CLIMATE

YI ZHANG

Abstract

This dissertation synthesizes long-standing theoretical ideas to develop quantitative constraints on several aspects of tropical climate, namely convection, heat stress, precipitation, and outgoing longwave radiation.

A zeroth-order picture of the tropical troposphere is that deep convection maintains a moist adiabatic temperature profile in the vertical and gravity waves quickly smooth any temperature gradients in the horizontal, which is formally known as convective quasi-equilibrium (QE) and the weak-temperature-gradient (WTG) assumption. We expect that strict QE-WTG should yield a uniform moist static energy (MSE) threshold for deep convection. Consistent with the theoretical expectation, we find that deep convection only occurs over the highest subcloud MSEs and that the convective subcloud MSE (daily-mean subcloud MSE weighted by precipitation) is roughly uniform between 20°S and 20°N. QE-WTG forces the highest subcloud MSEs to be equal over land and ocean, not only in the present climate but also in much colder and warmer climates.

The annual-maximum wet-bulb temperature, a metric for extreme heat stress, is also controlled by the QE-WTG dynamics due to the functional relationship of wet-bulb temperature with MSE. We provide a theoretical projection that the annual-maximum wet-bulb temperature will increase roughly uniformly by about 1°C for each 1°C of tropical mean warming. This result suggests that limiting the mean surface warming also limits heat stress extremes in the tropics.

QE-WTG controls the occurrence of deep convection and thus precipitation. Global climate models consistently predict that tropical precipitation will be distributed more unevenly in space with global warming. We show that the unevenness of precipitation can be traced back to the unevenness of subcloud MSE distribution. We then explain the change in sublcoud MSE distribution with a simple scaling accounting for the Clausius-Clapeyron increases of boundary-layer specific humidity under invariant relative humidities. The invariance of relative humidities also has implications for the linearity of outgoing longwave radiation with surface temperature.

Contents

Listing of figures

xiii

0
Introduction

This thesis includes some recent advances on several aspects of the Earth's tropical atmosphere – convection, precipitation, heat stress, and outgoing longwave radiation. We single out the tropics because the nature of the atmospheric motion in the tropics is different from that in the mid-latitudes. In the mid-latitudes, the quasi-balance between the Coriolis force resulting from the Earth's rotation and the pressure gradient force provides the

zeroth-order constraint for atmospheric motion. This constraint is weak in the tropics because the Coriolis force projects weakly onto the horizontal plane.

The tropical atmospheric motion is thus not the curling and swirling dye in rotating tank experiments, but it bears some similarity to the boiling water in one's kitchen. Heated water rises from the bottom of the pot making room for the sinking, cooler water, just like frequent deep convection in the tropical atmosphere brings surface air upward. However, tropical convection is different from boiling water in two ways. Convective instability in boiling water is produced by heating from below but is also produced by cooling throughout the tropical troposphere. CO_2 and water vapor in the atmosphere both interact strongly with radiation, resulting in a net cooling that has to be balanced by convective heating. Also, atmospheric convection is irreversible. A water parcel in the boiling pot can quickly (seconds, depending on the depth of the pot and the strength of the stove) sink back to the bottom as the same water parcel, but an air parcel brought up quickly (hours) by deep convection loses the condensed water along the way in the form of precipitation and cannot go down following the same path up. This dry air parcel then has to cool through radiation and sink slowly (tens of days) back to the surface. The strong asymmetry between upward and downward air velocity causes an approximately 1:1000 ratio between the area fractions that are unstable and stable to deep convection. The above description is the radiative-convective equilibrium, a useful starting point of conceptually thinking about the tropical atmosphere.

Although simulations of radiative-convective equilibrium and associated theoretical explanations have shed light on many important aspects of tropical atmospheric dynamics, there is still a long distance from these, mostly idealized, simulations to the observed

climate. Similar gaps between theory and reality can be found in all aspects of climate science, which is essentially due to the complexity of the climate system. Scientists, well aware of the existence of such knowledge gaps, build up understanding for real-world problems through a hierarchical approach – an approach by building a hierarchy of models of various degrees of complexities spacing between idealized theories and complex climate systems (Held, 2005). In understanding the tropical atmosphere, this thesis' work carries the same spirit as the hierarchical approach, but instead of building a hierarchy of models, I attempt to connect observations directly to established theories.

In the following chapters, I will first present the explorations of tropical precipitation observations at the early stages of my graduate study (Chapter 1), which inspired the ideas of Chapters 2 and 4. Readers interested in solid results could skip Chapter 1. Chapter 2 shows that a conceptual picture of tropical atmospheric dynamics comprising the convective quasi-equilibrium and the weak-temperature gradient assumptions can effectively unify the observed moist static energy in subcloud layers over land and ocean. Chapter 3 is an application of Chapter 2's results to heat stress, a concern of society. Chapter 4 presents a quantitative explanation for the increasingly uneven distribution of tropical precipitation with global warming. Chapter 5 addresses the radiative aspect of the atmosphere and shows why the global-mean outgoing longwave radiation is linear with the global-mean surface temperature despite the prominent super-greenhouse effect over some tropical oceans. In the end, I will conclude by summarizing the overall findings and discussing possible directions for future work (Chapter -1). Interested readers are encouraged to refer to the Supplementary Information of published versions of Chapters 2-5 for more technical details.

1

Precipitation and boundary-layer thermodynamic properties

1.1 LEAVING THE LATITUDE-LONGITUDE SPACE

The tropics show a wide variety of local climates ranging from rain forests to deserts as a result of varying precipitation rates across regions (Fig. 1.1). What controls the spatial dis-
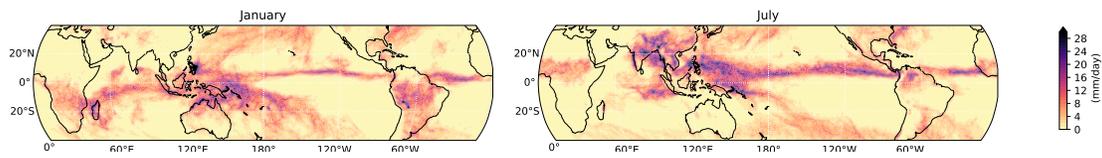
Figure 1.1: Precipitation climatology in January and July. Data shown are daily precipitation in January and July averaged over the period 2001-2004 from Tropical Rainfall Measuring Mission (Huffman et al., 2007).

tribution and temporal evolution of tropical precipitation is a fundamental problem in atmospheric dynamics. An extensive body of research has focused on the role of large-scale atmospheric circulations in controlling the occurrence of convection and precipitation. These circulations include the Hadley Cell, the Walker Cell, the Intertropical Convergence Zone (ITCZ), and monsoon circulations over subtropical land regions. Each of these circulations has a distinctive spatial pattern as a result of, at least to some degree, the Earth's rotation. The spatial patterns imply that whether a location receives precipitation is a matter of geographical location. However, the effect of the Earth's rotation is relatively weak in the tropics, compared to that in the extratropics. Rotation is what tells east from west, north from south; without a strong constraint from rotation, geographical location is less important. For the tropics, could something else be more important than location in determining whether a place receives precipitation? Could there be another meaningful way of inspecting tropical precipitation if we abandon the conventional map view? With these general questions, we start by graphing tropical precipitation, but not on a map.

Tropical rain band migrates in latitudes and longitudes with seasons (Fig. 1.1), but we are interested in whether this migration in space changes the total surface area receiving precipitation. We thus calculate how much area the most intense 90%, 50%, or 10% of total precipitation covers (Fig. 1.2a). The area is determined by sorting daily-mean precipitation intensities of all locations in the tropics in descending order and take the cumulative area
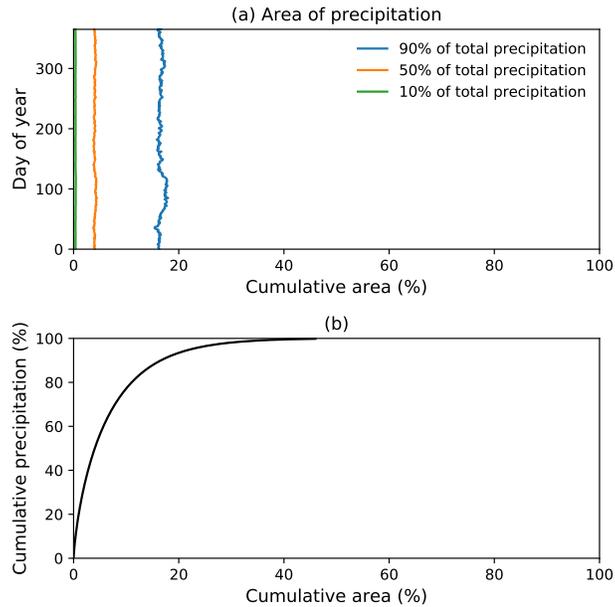
Figure 1.2: Area of 10%, 50%, and 90% of most intense precipitation for each day of year. Data shown are daily-mean precipitation data from TRMM 30°S-30°N.

that has received a certain percentage of total precipitation (Fig. 1.2b). 90% of total precipitation falls on only 18% of area, 50% on 4%, 10% on less than 1% – Daily-mean precipitation is very unevenly distributed in space. Interestingly, these area of precipitation only varies by a few percentages with the seasonal cycle, despite the evident spatial shift of rain bands shown in Fig. 1.1, and finding invariance in variables is always useful. In the next section, we will examine the relationship of precipitation with local thermodynamic states to shed more light on the invariant area of precipitation.

1.2 INTO SPACES OF THERMODYNAMIC VARIABLES

The theoretical ground for expecting a significant role of boundary-layer thermodynamic properties in controlling tropical convection is that the free-tropospheric temperature is

roughly horizontally uniform due to the smallness of the Coriolis parameter near the equator, known as weak temperature gradient (WTG) (Charney, 1963; Sobel & Bretherton, 2000), and, as a result, whether a location is unstable to convection largely depends on the thermodynamic property of the boundary layer underneath. Motivated by this concept, the study of tropical convection activity as a function of sea surface temperature (SST) dates back to decades ago. The average intensity of convection increases sharply when the underlying SST is above a threshold of around 27°C and then it strangely decreases as SST goes beyond 30°C (Zhang, 1993; Waliser & Graham, 1993). Later work argues that this decrease of precipitation with SST cannot be explained with thermodynamics alone, and other non-thermodynamic factors such as surface latent heat fluxes (Zhang & Mcphaden, 1995) or atmospheric intrinsic dynamics (He et al., 2018) have to be considered. However, the expected monotonic relationship between precipitation and SST is based on premises that may not hold. Therefore, the decrease of precipitation rate with SST is not enough to write off the role of thermodynamics. In the following, we will present a systematic exploration of the relationship between precipitation and boundary-layer thermodynamic properties.

We consider three thermodynamic state variables, namely SST, subcloud moist static energy, and an approximation to CAPE termed subcloud buoyancy (Williams & Pierrehumbert, 2017). Subcloud buoyancy is the most adequate variable to describe the column instability, followed by subcloud MSE and SST.

Subcloud buoyancy (B) B is defined as the difference between the moist static energy (MSE) in the subcloud layer (h_s hereafter) and the saturated MSE in the free troposphere

(h_a^*).

$$B = h_s - h_a^* \qquad (\text{1.1})$$

h_s is calculated as the average MSE between the surface and the lifting condensation level and h_a^* is calculated as the average saturated MSE between the lifting condensation level and the 300 hPa pressure level, where moist static energy h is calculated following the definition

$$h = c_p T + gz + Lq. \qquad (\text{1.2})$$

SUBCLOUD MSE (h_s)   If the free-tropospheric temperature is strictly uniform in the horizontal, then B can be reduced to subcloud MSE (h_s). Comparing tropical precipitation as a function of B and h_s elucidates the role of the departure from strictly uniform h_a^*. Note that B and h_s are defined over both land and ocean, but this is not the case for surface temperature, the last variable considered.

SEA SURFACE TEMPERATURE (SST)   Over the ocean, geopotential height variations are negligible, and relative humidity in the marine boundary layer is uniform; the same is not true for the land. Therefore h_s can be reduced to SST under these premises.

B and h_s are derived from 6-hourly reanalysis fields of temperature, specific humidity, and geopotential height on pressure levels from ERA-Interim (Dee et al., 2011) then averaged to the daily timescale. The lifting condensation level is calculated location-wise every 6 hours. Daily SST data from the NOAA 1/4° daily Optimum Interpolation Sea Surface Temperature (Reynolds et al., 2007) are interpolated to the resolution of ERA-Interim (0.75°x0.75°) with a bilinear algorithm. We use daily precipitation observations from Trop-
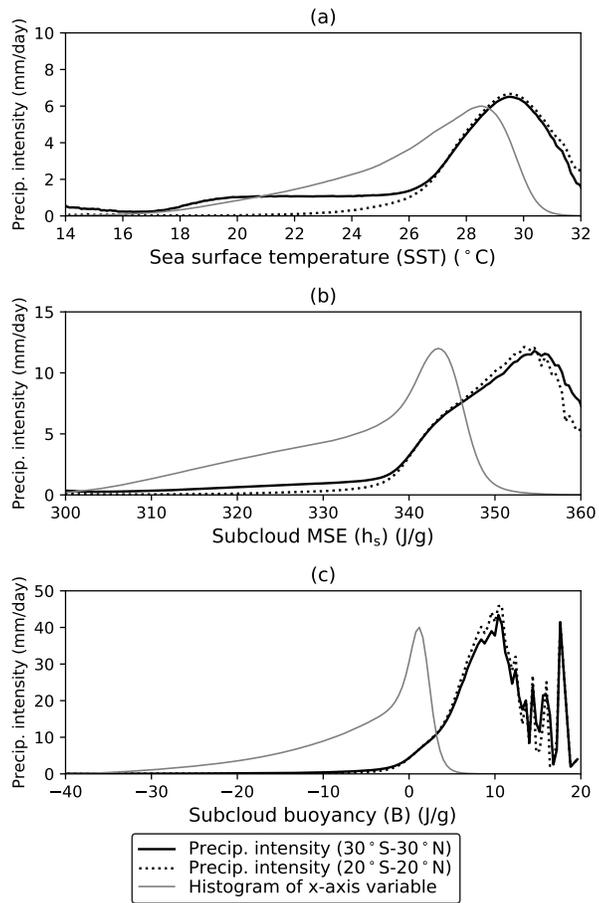
Figure 1.3: Mean precipitation intensity in spaces of thermodynamic state variables. Also shown is the frequency distribution (light grey) of each thermodynamic state variable.

ical Rainfall Measuring Mission (TRMM) (Huffman et al., 2007) aggregated to the ERA-Interim resolution conserving the total precipitation flux.

1.2.1 Precipitation distribution in spaces of thermodynamic variables

Fig. 1.3 shows the mean precipitation intensity as a function of SST, h_s and B. Up to about 30°C, precipitation intensity increases with SST. At SSTs higher than 30°C precip-
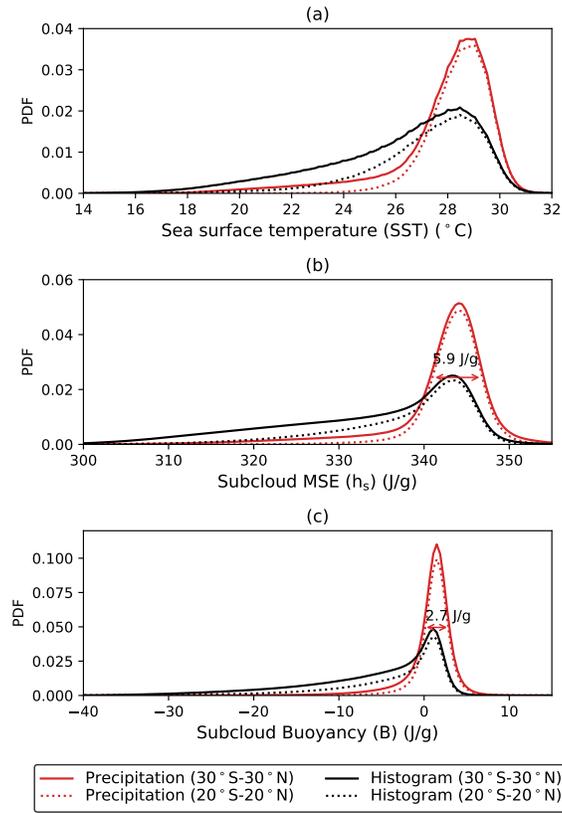
Figure 1.4: Precipitation distribution in spaces of thermodynamics variables. The distribution of precipitation as functions of thermodynamic variables (red lines) namely (a) sea surface temperature (SST), (b) subcloud moist static energy (h_s), and (c) subcloud buoyancy (B) and the corresponding histogram of each thermodynamic variable (black lines). The solid lines are for data between 30°S-30°N, and the dotted lines are for data between 20°S-20°N.

itation intensity decreases with SST, and about 10% of the tropical ocean is in this regime. Figs. 1.3b and c show that in h_s- and B-space, this peculiar regime of decreasing precipitation intensity still exists, however, the area fraction experiencing such regime is less than 0.1% of the tropics. The improved monotonic relationship of precipitation with h_s than SST suggests that relative humidity variations in the subcloud layer plays a role. The relative humidity near the ocean surface is always high, but the subcloud layer on average can be much dryer).

Fig. 1.4 shows precipitation fraction as a function of SST, h_s and B, as well as the probability distribution of these three variables. Precipitation fraction is calculated by binning daily-mean precipitation observations in SST bins of 0.1 K, subcloud MSE bins of 0.2 J/g, and subcloud buoyancy bins 0.2 J/g, adding up the precipitation in each bin then dividing the sum by the total precipitation in the tropics. Tropical SST has a skewed distribution covering a wide range of values from well below 20°C to above 30°C, but the precipitation distribution is much narrower and restricted to the high SST values – More than half of the oceanic precipitation occurs where SST is above 28°C (Fig. 1.4a). Similarly, precipitation is restricted to the high ends of h_s (Fig. 1.4b) and B (Figure 1.4c) distribution. A small fraction of precipitation can occur at very low SST or h_s indicated by the thin left tail of the distribution in Fig. 1.4a and b. This part of the precipitation distribution is mainly induced by extratropical eddies rather than tropical deep convection, a point we will come back to in Chapter 2. The characteristic width of the precipitation fraction peak, expressed in terms of the full-width at half-maximum (FWHM) is 6.0 J/g in h_s-space and 2.8 J/g in B-space. The FWHM in B is comparable to the typical value of convective available potential energy (CAPE) of 2 J/g (Williams & Renno, 1993; Gettelman et al., 2002), indicative of the sufficiency of B for our purpose of climatological analysis. The difference by a factor of two between these two FWHM in h_s- and B-space suggests a prominent role of the horizontal free-tropospheric temperature gradients (or h_a^*).

To enable comparison of different thermodynamic variables, we modify Fig. 1.2b in such a way that it shows the proportion of precipitation received by the top x% of the area when precipitation data are sorted according to SST, h_s, or B (Fig. 1.5). Fig. 1.5 allows a convenient comparison of different thermodynamic variables and provides an intuitive vi-
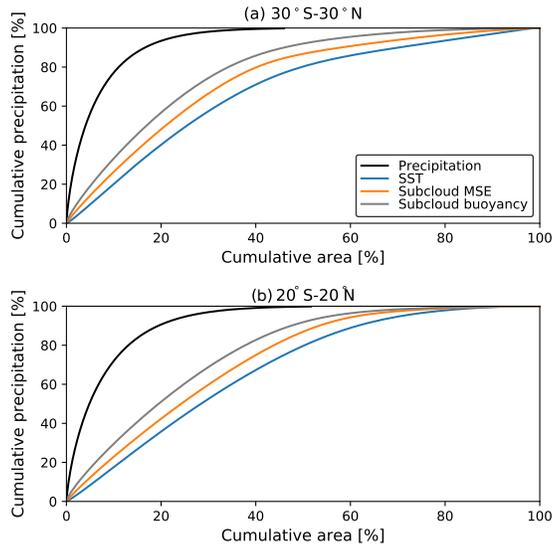
Figure 1.5: Cumulative precipitation as a function of cumulative area.

sualization of how much can be explained by the thermodynamics – If the thermodynamic variable has a deterministic relationship with precipitation, the resulting curve would be the same as the original curve when precipitation data are sorted according to itself; If the thermodynamic variable does not provide any information on the precipitation distribution at all, the resulting curve would be a straight line from (0,0) to (1,1). The three thermodynamic variables are all between these two extreme situations. It takes 17% of the area to collect 90% of total precipitation while it takes the top 48% of B, top 60% of h_s, and top 72% of SST to collect 90% of precipitation, all of which are much larger than the 17%.

1.2.2 THE LACK OF SEASONALITY IN CONVECTIVE REGIONS

Since all three thermodynamic variables can explain precipitation intensity to some degree (Fig. 1.5), we look into the distribution of those thermodynamic variables for clues
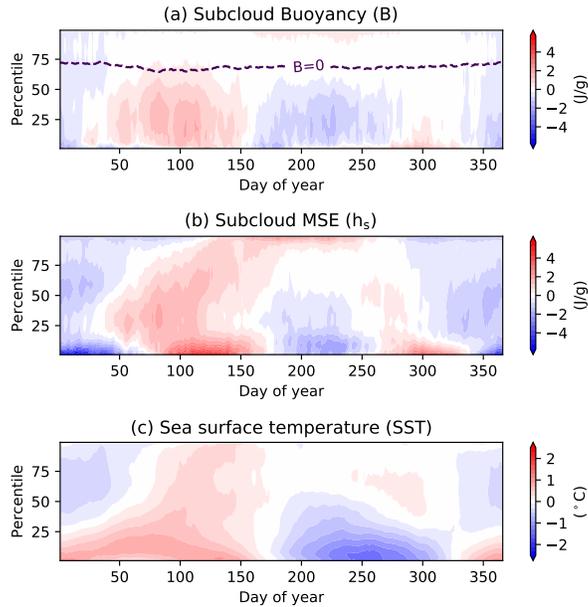
Figure 1.6: The seasonal evolution of the thermodynamic variables in percentiles. The annual means for each percentile are subtracted. The dashed black line in (a) shows where the zero B is.

on the lack of seasonality of the area of precipitation (Fig. 1.2a). Figure 1.6a shows the B percentiles throughout the seasonal cycle with the annual mean for each percentile sub-tracted to isolate the anomalies. The area of positive B is around 25% throughout the year (dashed black line in Fig. 1.6a), within which the B distribution is largely invariant with seasons. While we don't make a causual argument that the invariance area of positive B leads to the invariance area of precipitation, this phenomenon is an interesting one that needs to be better understood. A seasonal cycle is visible in the lower 75% of the area with negative B, however, these regions are stable to convection receive little precipitation. For subcloud MSE (Fig. 1.6b) and SST (Fig. 1.6c), the seasonality is also more visible in the bottom percentiles than in the top percentiles. The "warmest" regions in the tropics appear to be rather insensitive to the varying solar forcing with seasons.
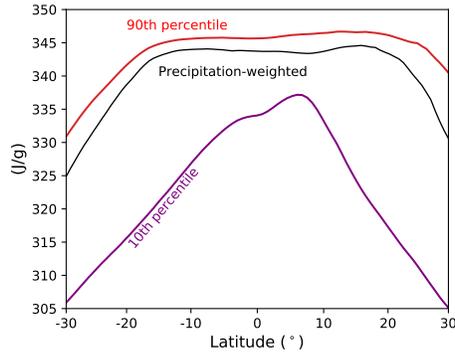
Figure 1.7: The high and low percentiles and the precipitation-weighted mean of subcloud MSE as a function of latitude. The 10th and 90th percentile of subcloud MSE are first taken for each year then averaged over 2001-2014. The precipitation-weighted subcloud MSE is also first calculated for each latitude and each year then the multiyear average is taken. Daily-mean subcloud MSE derived from ERA-Interim and daily-mean precipitation observation from TRMM is used.

The percentile figure (Fig. 1.6) is abstract and some extra dimension of the space is helpful to our understanding. We show the 10th and the 90th percentile of sublcoud MSE at each latitude along with the convective MSE in Fig. 1.7. The convective (subcloud) MSE is calculated by weighting the daily-mean subcloud MSE at each gridbox with the corresponding rainfall received, following the precipitation-weighting method first introduced in Flannaghan et al. (2014).

$$\text{Convective subcloud MSE} = \frac{\sum_i P_i h_{si}}{\sum_i P_i} \tag{1.3}$$

This figure contains much non-trivial information: First, the convective MSE is nearly uniform in the deep tropics, indicating that precipitation on average occurs at the same subcloud MSE across those latitudes. Since precipitation is a proxy for convective mass flux, another way to interpret this is that the average MSE of air brought up by convection is the same at each latitude. Second, the 90th percentile of subcloud MSE exhibit strong

14

equator-to-pole gradients, however the 10th percentile is roughly uniform – There appears to be a spatially uniform upper bound on subcloud MSE. Third, the 10th percentile of subcloud MSE is close to the precipitation-weighted MSE, indicating that convection occurs at top subcloud MSEs. Connecting Fig. 1.7 with the percentiles of subcloud MSE shown in Fig. 1.6b, convection occurs at the largely invariant top MSE percentiles, and the rainband moving north and south with seasons thus results in a uniform precipitation-weighted MSE.

1.3 WHAT IS INVARIANT ABOUT TROPICAL PRECIPITATION

The exploration of tropical precipitation and thermodynamic variables presented in this chapter is complementary to the conventional view of presenting precipitation on a map. This chapter is phenomenological, but it has fueled the ideas of the following chapters. To conclude this chapter without a solid conclusion, I summarize a few things that are invariant about tropical precipitation in an annual cycle:

1. The area fraction of precipitation. However, in Chapter 4, we will show that this area changes with warming.

2. The area fraction of positive subcloud buoyancy.

3. The precipitation-weighted MSE. The uniform precipitation-weighted MSE in Fig. 1.7 becomes interesting once we separate land and ocean, which is to be discussed in the following Chapter.

2

The Quasi-Equilibrium and Weak Temperature Gradient Framework

2.1 Two cornerstones of tropical atmospheric dynamics

CONVECTIVE QUASI-EQUILIBRIUM (QE)   Convective quasi-equilibrium is originally proposed by Arakawa & Schubert (1974) as a closure assumption for a parameterization

16

of convection. Over the decades that follow, the importance of QE is recognized in constructing theories of tropical large-scale atmospheric circulations, and multiple versions of QE have been developed (e.g. Betts, 1986; Emanuel et al., 1994; Raymond, 1995; Emanuel, 2007). The most strict version of QE requires that moist convection always maintain a moist adiabatic temperature profile and the neutral buoyancy of air lifted from the sub-cloud layer to levels above. Relaxed versions of QE allow the actual atmosphere to be relaxed toward the strict QE state over some time scale.

WEAK TEMPERATURE GRADIENTS (WTG) The weak temperature gradient assumption states that the free troposphere cannot sustain substantial horizontal temperature gradients due to the smallness of the Coriolis parameter in the tropics (e.g., Charney, 1963; Sobel & Bretherton, 2000), and a direct consequence of WTG is that on large scale the dominant balance is between heating and vertical advection of potential temperature (e.g., Sobel et al., 2001). While QE is used to parameterize small-scale convection, the weak temperature gradient assumption is used to parameterize the large-scale circulation when the focus of the simulation is on convective scale (e.g., Sobel & Bretherton, 2000; Raymond & Zeng, 2005).

THE QE-WTG FRAMEWORK In our QE-WTG framework, the tropical troposphere can be seen as consisting of a boundary layer with diverse temperature, humidity, and topography (the three components of MSE) and a free troposphere that is comparatively homogeneous. Deep convection transports boundary layer air upward into the free troposphere. Once the free troposphere is filled with buoyant air originating from the warm and humid boundary layer, it suppresses upward motion in the colder regions, establishing a threshold for convection. Consequently, at the limit of strict quasi-equilibrium and zero temperature

gradient, simultaneously convecting regions, regardless of over land or ocean, should have the same subcloud MSE which we refer to as the MSE threshold for convection (Fig.2.1).

$$h^*_{a,1} \;\overline{\underline{\quad\text{WTG}\quad}}\; h^*_{a,2}$$

$$\text{QE} \;\|\| \qquad\qquad\qquad \text{QE}\;\|\|$$

$$h_{s,1} \;\overline{\overline{\quad\text{QE-WTG}\quad}}\; h_{s,2}$$
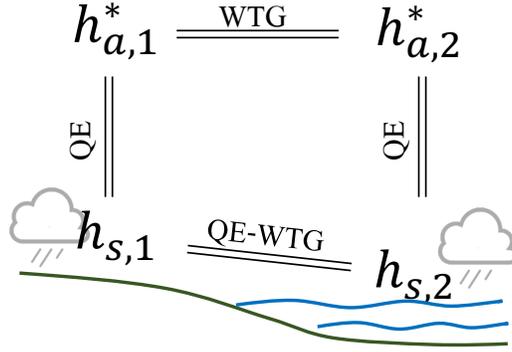
Figure 2.1: Schematic of the QE-WTG framework. QE denotes convective quasi-equilibrium, and WTG denotes weak temperature gradients. h_s denotes subcloud MSE, and h^*_a denotes the saturated MSE averaged in the free troposphere. Subscripts indicate two different locations that could be far apart and could be over either land or ocean.

Our QE-WTG framework is inspired by previous work inspecting the tropical troposphere from similar angles. Joshi et al. (2008) note that in model calculations there exists a level sufficiently high up in the troposphere where temperature change in response to forcing is similar over land and ocean, and the larger surface temperature response over land then is consistent with the different changes in lapse rates over land and ocean. Byrne & O'Gorman (2013a) formulate this effect in terms of the equality of equivalent potential temperature averaged over land and ocean as a result of weak temperature gradients in the free troposphere and convective quasi-equilibrium, which is largely supported by simulations with idealized climate models. However, they also notice that this equality breaks down in realistic climate models (Byrne & O'Gorman, 2013b), and the changes in the mean surface equivalent potential temperature, rather than the mean equivalent potential temperatures themselves, are more similar over land and ocean (Byrne & O'Gorman,

2013b, 2018).

In the following, we present observations and model results to provide a more precise picture than previous work of how tropical atmospheric dynamics couple the subcloud MSE over land and ocean to the free troposphere.

2.2 THE MSE THRESHOLD FOR CONVECTION: A ZEROTH-ORDER PICTURE

While previous studies (Byrne & O'Gorman, 2013a,b, 2018) evaluate the QE-WTG picture with the large-scale mean MSE over land and ocean, we argue that QE-WTG should be evaluated only in the regions where deep convection couples the MSE in the subcloud layer to the free troposphere and does not apply to the regions where the sublcoud MSE is too low to reach the threshold for convection. Leveraging the precipitation-weighting method in Section 1.2.2, we can show that QE-WTG apply to each latitude in the observations, even on a daily timescale, and there is a clear breakdown of the theoretical picture around 20° in both hemispheres.

The zonal-mean subcloud MSE (Fig. 2.2a) peaks around the equator reflecting the annual-mean solar forcing, whereas the convective subcloud MSE (Fig. 2.2b) is roughly uniform throughout the inner tropics and very similar between land and ocean, reflecting the weak horizontal temperature gradients in the free troposphere. The sharp drop-off at about 20° in both hemispheres indicates where the Coriolis effect is no longer negligible and QE-WTG breaks down. As a result, precipitation in the subtropics can occur either at very low subcloud MSE when induced by the extratropical eddies (Funatsu & Waugh, 2008) or at very high subcloud MSE during the South Asian monsoon which creates the peak in the convective MSE around 25°N over land (Boos & Kuang, 2010). Using sub-
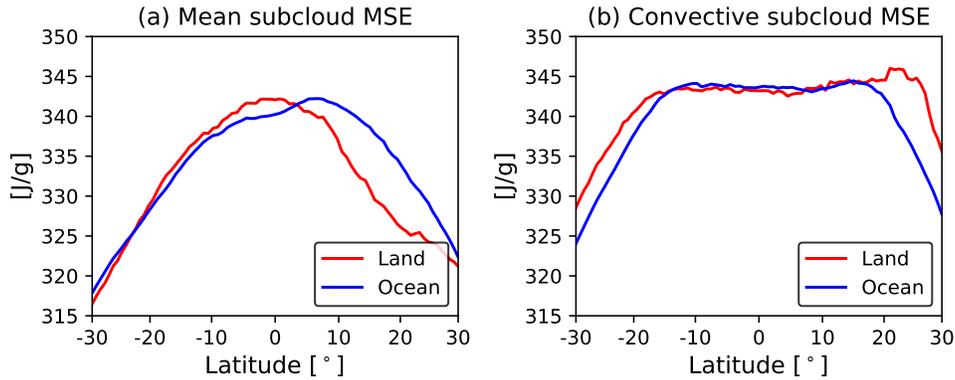
Figure 2.2: Zonal-mean (a) and convective (b) subcloud moist static energy (MSE) over land (red) and ocean (blue). Subcloud MSE is derived from ERA-Interim and precipitation is from TRMM. Daily data from 2001 to 2014 are used. The convective subcloud MSE is determined by weighting the subcloud MSE at each longitude with the corresponding precipitation within each latitudinal band of $0.75°$ wide.

cloud MSE derived from MERRA2 instead of ERA-Interim does not change this result. The contrast between the mean and the convective subcloud MSE resolves the aforementioned inconsistency between the strict QE-WTG theory and the realistic simulations mentioned in Byrne & O'Gorman (2013b). Convection only occurs in the part of the domain where the subcloud MSE is high enough to reach the tropically uniform MSE threshold of about 343 J/g shown in Fig. 2.2b, and in the part of the domain that is not convecting subcloud MSE is not coupled to the free troposphere and therefore can differ between land and ocean.

The calculation of subcloud MSE deserves some description. The common threshold MSE over land and ocean emerges clearly if the monthly mean MSEs averaged from 925 hPa to 1000 hPa are weighted by monthly precipitation. However, convection occurs on the timescale of hours, and to not leave anything to chance subcloud MSE is calculated as follows: We calculate the lifting condensation level (LCL) as the pressure level closest to the

first saturation point of an adiabatically lifted surface parcel on a 6-hourly time frequency for every location and compare the LCLs to the 6-hourly boundary layer heights from ERA-Interim. Subcloud MSE is then the average MSE either within the layer between the ground and the LCL when the LCL is within the boundary layer. Over dry land, the LCL can be in the middle troposphere which doesn't make sense. In this case, the boundary-layer height from ERA-Interim is used. The 6-hourly subcloud MSE is averaged to a daily timescale to match the time resolution of the precipitation observation.

A more stringent test examines how effectively QE-WTG works on daily timescales. Fig. 2.3 shows the seasonal evolution of the zonal-mean subcloud MSE in the convective regions (left column) and non-convective regions (right column) over land (lower row) and ocean (upper row). Here the convective MSE is defined as the mean subcloud MSE where the rain rate is above 6 mm/day (Sobel et al., 2002) and *vice versa* for the non-convective MSE. The results are not sensitive to the choice of a precipitation threshold from 2 mm/day to 20 mm/day. This method is different from the precipitation-weighting method used in Fig. 2.2 but yields similar convective MSE values, essentially because precipitation anywhere in the inner tropics occurs at very similar subcloud MSE. To facilitate the comparison, a reference value for each day of year, calculated as the mean subcloud MSE in the convective regions over equatorial (5°S-5°N) ocean, is subtracted. Even on a single day of year, the convective MSE is still uniform over a broad range in latitude, though this latitudinal range has seasonality (Fig. 2.3, right column). Within 20°S-20°N, the seasonal evolution of the non-convective MSE has more prominent land-ocean contrast than the convective MSE (indicated by the shapes of the dashed black contours), supporting the concept that only the subcloud MSE in the convective regions over land and ocean are tied
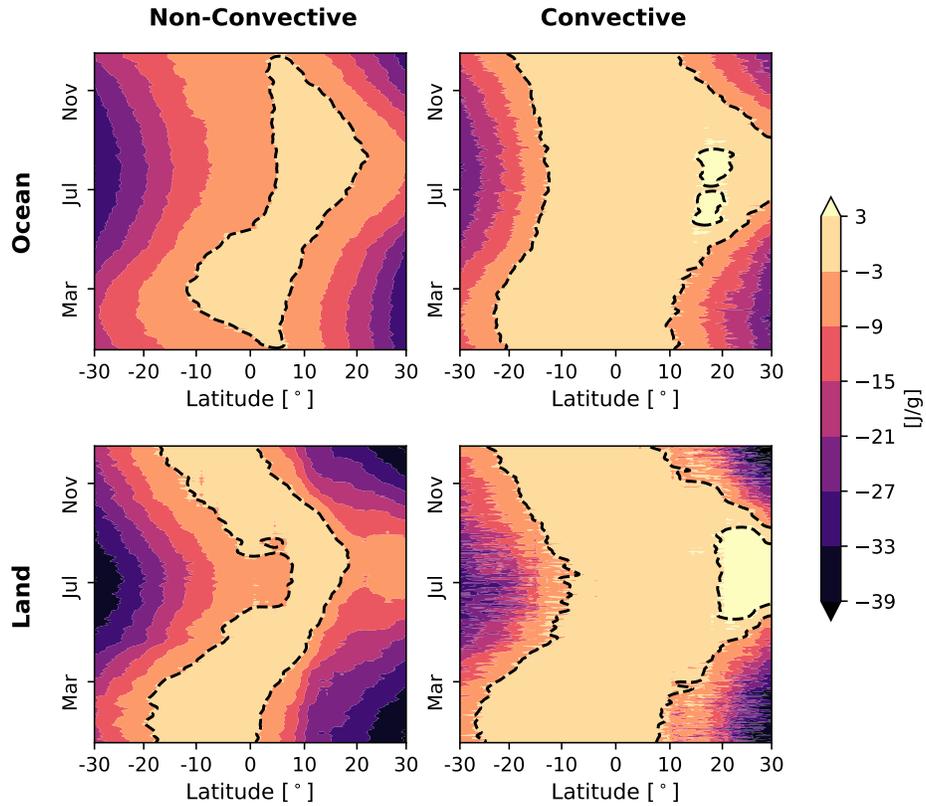
Figure 2.3: The mean subcloud moist static energy (MSE) as a function of latitude and day of year in the non-convective and convective regions over ocean and land. A reference value for each day of year, calculated as the mean subcloud MSE in the convective regions over equatorial (5°S-5°N) ocean, is subtracted from all panels. Daily data are used from ERA-Interim and TRMM between 2001 and 2014. Convective and non-convective regions are identified with a precipitation threshold of 6 mm/day. The dashed contour lines indicate the subcloud MSE within ± 3 J/g relative to the common reference value.
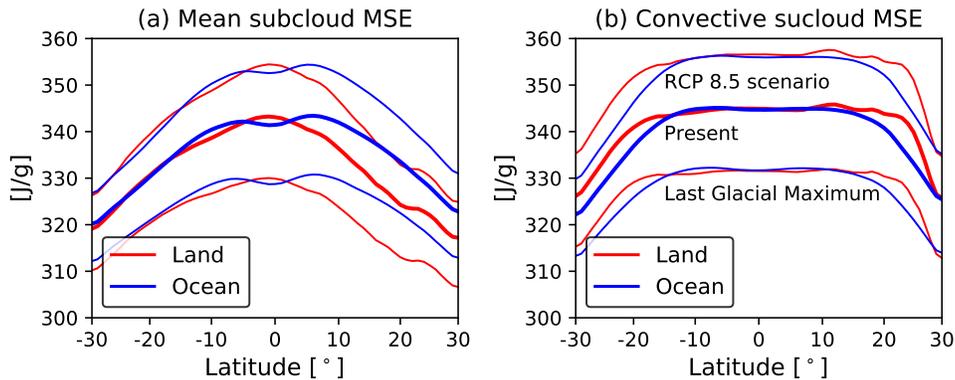
Figure 2.4: Zonal-mean (a) and convective (b) subcloud moist static energy (MSE) for model simulations. The multi-model mean of monthly data from CMIP5 models are shown. Three experiments are shown from bottom to top: the Last Glacial Maximum, the period from 1979 to 2005 in the simulation of current climate (labeled "Present"), and the last 20 years of the 21st century in the global warming simulation (labeled "RCP 8.5 scenario").

to the uniform temperature in the free troposphere.

The physics involved in the QE-WTG mechanism does not rely on the mean climatic state, therefore QE-WTG is expected to hold in all climates. Global climate models from the Coupled Model Intercomparison Project phase 5 (CMIP5) (Taylor et al., 2012) that correctly reproduce the observed uniform convective MSE in the simulations of the present climate also show a uniform convective MSE in the projections of a much warmer climate under the Representative Concentration Pathway 8.5 (RCP8.5) emission scenario (Fig. 2.4). Model simulations of the much colder Last Glacial Maximum also show a uniform convective MSE over both land and ocean. Therefore, Fig. 2.4 demonstrates the validity of QE-WTG in a wide range of climates.

2.3 Finite width of the MSE threshold: a first-order correction

The latitudinal uniformity of the convective subcloud MSE in the inner tropics and its similarity between land and ocean (Fig. 2.2, 2.3) provide observational support for the zeroth-order picture. However, it is well established that factors such as the mid-tropospheric humidity (Emanuel, 2019; Brown & Zhang, 1997), convective inhibition (Mapes, 2000), low-level convergence (Lindzen & Nigam, 1987; Back & Bretherton, 2009), and stationary or transient equatorial waves (Gill, 1980; Kiladis et al., 2009) all affect the triggering of convection. How can these complicating factors be reconciled with the simple picture of a uniform MSE threshold for convection?

The convective MSE threshold shown in Fig. 2.2b is a weighted mean over a range of subcloud MSE values rather than a single MSE value. Fig. 2.5a shows the fraction of precipitation that falls into each subcloud MSE bin of a width of 0.2 J/g. This precipitation distribution can be roughly regarded as the convective mass flux distribution as a function of subcloud MSE. If QE-WTG were strict, this distribution would be a Dirac function at the highest subcloud MSE. In the observed climate, however, the majority of precipitation occurs around 343 J/g–the value is comparable to the convective MSE (Fig. 2.2a)– with a Half Width at Half Maximum (HWHM) of 3 J/g. The half width of 3 J/g then encapsulates the previously mentioned factors that affect the local triggering of convection. This width is narrow compared to the entire range of the tropical subcloud MSE of about 60 J/g. Remarkably, the shape of the precipitation distribution as a function of subcloud MSE is also similar between land and ocean, a result not predicted by the theoretical limit of QE-WTG.
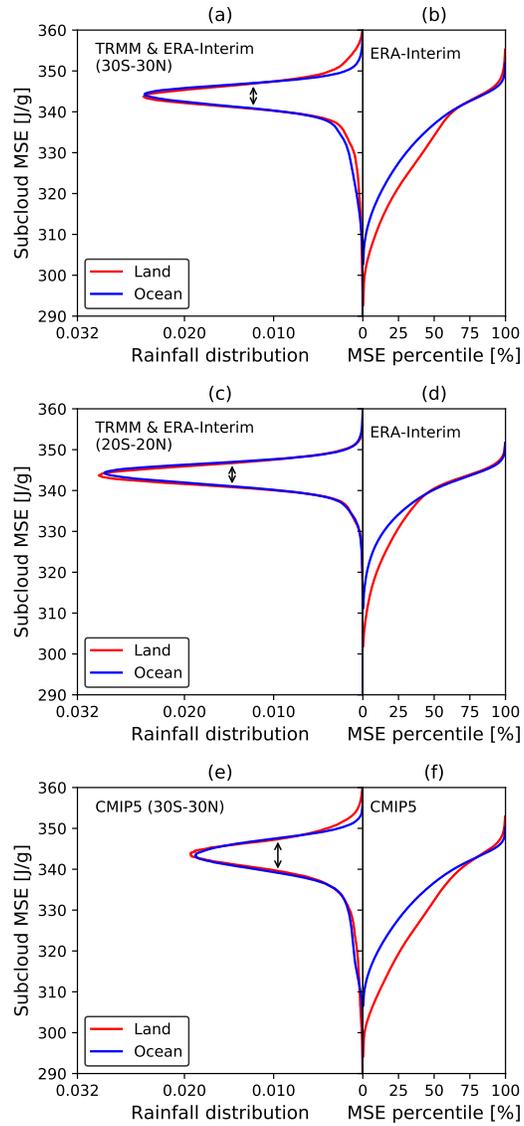
Figure 2.5: precipitation distribution as a function of subcloud MSE (left panels) and the corresponding percentiles of subcloud MSE (right panels). (a) and (b) show precipitation from TRMM and subcloud MSE from ERA-Interim between $30°$S and $30°$N. (c) and (d) are the same as (a) and (b) but with data between $20°$S and $20°$N. (e) and (f) are the same as (a) and (b) but is the multi-model mean of monthly output from CMIP5 models in the coupled simulation from 1979 to 2005 (Table S1). The double arrows indicate where the HWHM is evaluated.

The tails of the precipitation distribution at very high subcloud MSE above 350 J/g and low subcloud MSE below 336 J/g are somewhat different for land and ocean, due to the break-down of QE-WTG in the subtropics. When the latitudinal range is restricted to 20°S-20°N (Fig. 2.5c), the tails disappear and a convective mode centered at 343 J/g emerges which is almost identical over land and ocean.

Fig. 2.5e is the same as Fig. 2.5(a) but for the CMIP5 multi-model mean. The width of the MSE threshold is wider than that in the observations, because it is an average of models with slightly different mean states. In fact, the half width for an individual CMIP5 model is also 3 J/g on average. Limiting the latitudinal range to 20°S-20°N for the CMIP5 models results in better agreement between land and ocean (not shown) similar to the observational result (Fig. 2.5c,d).

To put the magnitude of the width into context, we compare it with typical MSE changes due to departure from the strict QE-WTG: Observed convective available potential energy (CAPE) varies between 0 and 4 J/g (Williams & Renno, 1993; Gettelman et al., 2002) and the free tropospheric temperature varies by order 1 K horizontally which translates to about 2 J/g of subcloud MSE. It is thus not obvious which factor contributes more given the similar amplitudes. We also notice that the width is not strongly dependent on the time frequency (daily or monthly) of data.

Figs. 2.5b,d,f show the corresponding percentiles of subcloud MSE sorted in ascending order and averaged in equal-area bins. Fig. 2.5b reiterates that only the highest subcloud MSE values between 30°S and 30°N are coupled over land and ocean while the low subcloud MSE values are free to differ – the upper 30% of subcloud MSE has almost identical distributions over land and ocean while the lower 70% of the subcloud MSE over ocean is

systematically higher than that over land. In addition, Figs. 2.5b,d highlight an interesting aspect of the Earth's tropical climate: The convective area fraction is approximately equal over land and ocean.

2.4 Conclusion and Implication

We show that a simple theoretical picture of the tropical troposphere based on the convective quasi-equilibrium and the weak-temperature-gradient assumptions (QE-WTG) can effectively explain the observations. In accordance with QE-WTG, the convective subcloud MSE is roughly constant with latitude between 20°S and 20°N on a daily timescale in the observed current climate and the simulated past and future climates. The utility of QE-WTG is manifested in its capability of reconciling the land-ocean contrast. The vastly different land and ocean surfaces share almost identical convective subcloud MSE, distribution of highest subcloud MSE values, and precipitation distribution as a function of subcloud MSE. These results fill the gap between the idealized, conceptual understanding of the tropical atmospheric dynamics and the real world consisting of diverse regional climates.

Whereas the role of subcloud MSE forcing the free troposphere has been well appreciated in tropical convection, we demonstrate that the horizontally uniform free tropospheric temperature forces the highest subcloud MSE values to be similar over land and ocean, which is an interesting aspect of convection in the tropics.

If I have to summarize this work in one sentence, it should go as follows: Convective quasi-equilibrium applies to convective regions but not to non-convective regions – almost a ludicrous tautology. However, this distinction changes how we understand the constraint

from QE-WTG on subcloud MSE. Before, the large-scale mean and annual average of MSE is considered to be approximately equal over land and ocean, but we show that it is the local, maximum MSE on the timescale of a day (or even a couple of hours) to be approximately equal over land and ocean. This shift from mean to maximum, from annual average to subdaily values, from large-scale mean to each location has implications for extreme heat stress projection, which is to be discussed in the following chapter.

3

Projection of Extreme Heat Stress

3.1 Why wet-bulb temperature

Extreme heat under global warming is a concerning issue for the growing tropical population. The most widely used metric for extreme heat has been the extreme temperature. However, projections of extreme temperatures have large regional uncertainty arising from insufficient model representation of important land processes (Vogel et al., 2017). More-

over, to facilitate the estimation of heat-induced health impact (or heat stress), the effect of humidity should also be included (Kovats & Hajat, 2008; Mitchell et al., 2016), and this is because the major way for humans to lose metabolic heat in hot weather is evaporative cooling (sweating) (Hardy et al., 1938; Hardy & Stolwijk, 1966), the efficiency of which anti-correlates with humidity. In particular, the inclusion of humidity is necessary for assessing heat stress in the tropics, the warmest and the most humid places on the Earth.

The importance of humid heat has been increasingly recognized (Mora et al., 2017; Sherwood, 2018). Studies have shown that increased humidity with temperature following the Clausius-Clapeyron relationship can worsen summer heat stress in the tropics (Delworth et al., 1999; Willett & Sherwood, 2012), while other work has noticed a reduction in either relative humidity (Fischer & Knutti, 2013) or specific humidity (Coffel et al., 2019) on the hottest days (not limited to the tropics). Given the possibility that humidity can interact with temperature in extreme heat, it is necessary to better quantify and improve our mechanistic understanding of the control of humid heat.

Here, we use the extreme wet-bulb temperature (TW), an integrated temperature-humidity metric for heat stress (see Methods). TW by definition is the lowest temperature that human skin can be cooled to through evaporation of sweat. Therefore, the closer TW is to the upper limit of human skin temperature (around $35°C$), the more intolerable the heat is, with a survival limit of TW=$35°C$ (Sherwood & Huber, 2010) (Note that high TW values below this survival limit also have adverse health impact). Furthermore, TW is a major component in the wet-bulb globe temperature (WBGT; See Methods) (ISO, 2017) which is the standard metric for workplace heat stress.

In this chapter, we argue that the regional extreme TW in the tropics is mainly con-

3. During local summer, TW increases and hits the bar. This triggers deep convection, which stops TW from increasing.

1. Deep convection over ocean sets the free-tropospheric temperature, which acts as a TW bar for the entire tropics.

High TW
High TW
High TW
High TW
Low TW
Low TW

2. During local winter, TW is below the bar and does not trigger deep convection.

4. Global warming lifts the TW bar uniformly.

Figure 3.1: Schematic of the mechanism controlling land $\mathrm{TW_{max}}$.

trolled by robust atmospheric dynamics that have been established previously (Byrne & O'Gorman, 2013a,b, 2018; Zhang & Fueglistaler, 2020), rather than local processes that are of more uncertainty. Therefore, tropical extreme TW can be robustly projected on regional scales under global warming.

3.2 Predicting land by predicting the ocean (theory)

For a theoretical projection of $\mathrm{TW_{max}}$, we argue that tropical atmospheric dynamics exert a strong, tropics-wide control on local $\mathrm{TW_{max}}$. This control is through the functional relationship between TW subcloud MSE (h_s):

$$h_s(z = 0) = c_p T + Lq = c_p \mathrm{TW} + Lq_{sat}(\mathrm{TW}), \tag{3.1}$$
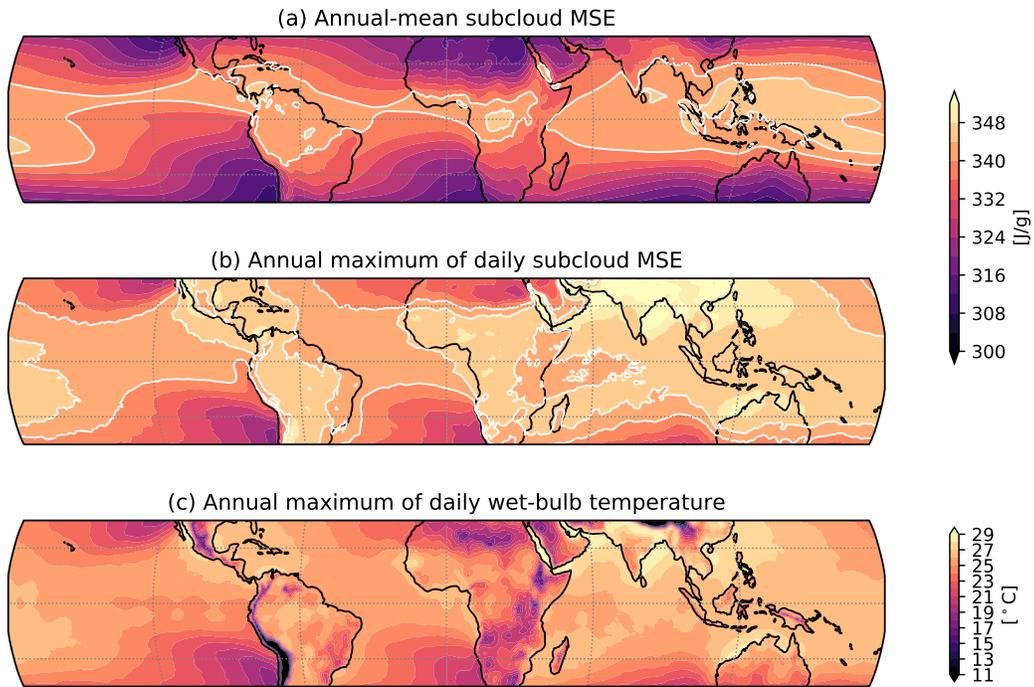
Figure 3.2: Maximum MSE is more uniform than the mean MSE. The annual-mean (a) and annual-maximum (b) daily-mean subcloud MSE and the annual-maximum daily 2-m wet-bulb temperature (c). Data are based on ERA-Interim from 2001-2014. White contours in (a) and (b) are to aid the comparison (The standard deviation is 8.8 J/g for panel (a) and 5.8 J/g for panel (b).)

where T and q are the temperature and the specific humidity (One can compare the left hand side of Eq. 3.1 with the definition of MSE in Eq. 1.2). In the tropics, the free-tropospheric temperature is roughly uniform in the horizontal as a result of the weak effect of the Earth's rotation. This horizontally uniform temperature, which is determined by the near-surface MSE in regions of deep convection, sets the upper bound for MSE at all locations. Indeed, the maximum near-surface MSE is roughly uniform within 20°S-20°N (even more uniform than the time-mean MSE; Fig. 3.2a,b), and the spatial pattern of TW_{max} closely follows the uniformity of the maximum MSE (Fig. 3.2c). As this upper bound for near-surface MSE and, equivalently, for TW is a common one over land or over ocean (Zhang & Fueglistaler, 2020), we expect that changes in TW_{max} should also be roughly equal over land and over ocean under global warming:

$$\Delta TW_{max,Land} \approx \Delta TW_{max,Ocean} \qquad (3.2)$$

Eq. (3.2) thus provides a handle on TW_{max} over land which is challenging to predict due to various land types and land processes, as a theoretical projection for TW_{max} over the ocean can be made relatively easily. Near the ocean surface, the air is close to saturation and TW changes are approximately equal to temperature changes (exactly equal when air is saturated), and $\Delta TW_{max,Ocean}$ is thus approximately equal to the change in the warmest SSTs. Therefore, 1°C of $\Delta TW_{max,Land}$ is accompanied by 1°C of warming of the warmest SSTs according to Eq. (3.2):

$$\Delta TW_{max,Ocean} \approx \Delta SST_{max} \qquad (3.3)$$

Furthermore, the relatively constant shape of SST histogram under global warming and interannual variability (Sobel et al., 2002) together result in a 1:1 correspondence between warming of the warmest SSTs and the mean SST warming:

$$\Delta\text{SST}_{\text{max}} \approx \Delta\overline{\text{SST}} \qquad (3.4)$$

Finally, the ocean covers 80% of area in the tropics, and therefore the tropical mean warming is dominated by mean SST warming:

$$\Delta\overline{\text{SST}} \approx \Delta\overline{T} \qquad (3.5)$$

Combining Eq. 3.2-3.5, we thus expect $\Delta\text{TW}_{\text{max,Land}}$ roughly equals the tropical mean warming.

3.3 Global climate model projections

Fig. 3.3a shows the projections of extreme TW (TW_{max}) and extreme temperatures (T_{max}) by 22 global climate models from the Coupled Model Intercomparison Project phase 5 (CMIP5) (Taylor et al., 2012) under the Representative Concentration Pathway 8.5 (RCP 8.5) emission scenario (Note that TW_{max} and T_{max} mostly refer to the annual maximum of *daily* mean values in this paper, and refer to the annual maximum of *3-hourly* values when specifically stated). The multi-model mean of T_{max} averaged over tropical land within 20°S-20°N warms faster than the tropical mean temperature. However, TW_{max} closely follows the tropical mean warming, similar to an earlier finding using an atmospheric model coupled to a slab ocean (Sherwood & Huber, 2010). These results also hold
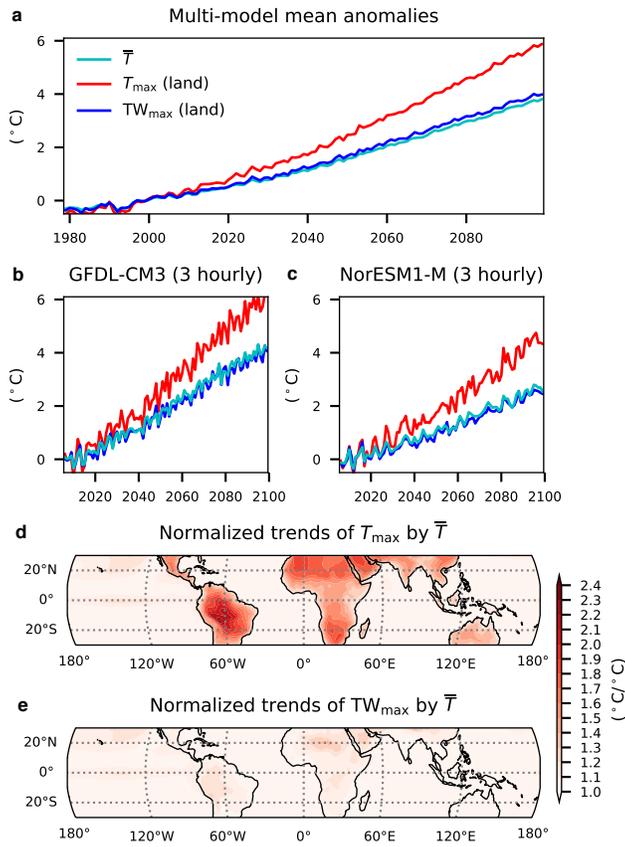
Figure 3.3: $\mathrm{TW_{max}}$ **and** T_{max} **trends in climate models under RCP 8.5. a,** Multi-model-mean time series of the tropical-mean (20°S-20°N) temperature ($\overline{T}$; cyan), land-mean T_{max} (red), and land-mean $\mathrm{TW_{max}}$ (blue). **b** and **c,** The same as **a** but using the annual-maximum 3-hourly values for T_{max} and $\mathrm{TW_{max}}$ for two individual models. **d** and **e,** Multi-model-mean location-specific T_{max} and $\mathrm{TW_{max}}$ trends normalized by $\overline{T}$ trends.
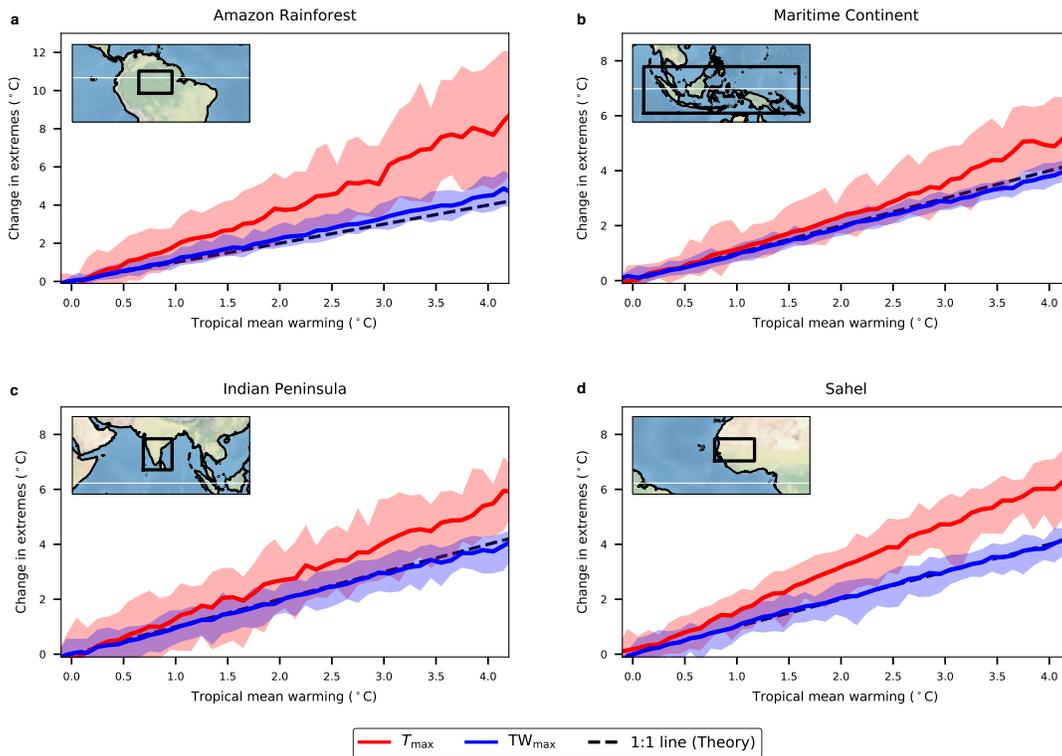
Figure 3.4: Model agreement on regional $\mathrm{TW_{max}}$ projections. Multi-model means (lines) and spreads (2.5-97.5th percentiles; shading) for regional T_{max} (red) and $\mathrm{TW_{max}}$ (blue) as a function of the tropical mean warming are shown for four regions, namely **a** Amazon rainforest, **b** Maritime Continent, **c** Indian Peninsula, and **d** Sahel (Only land data within the black frames on the maps are sampled). The dashed black lines indicate the 1:1 ratio.

when analyzing 3-hourly data that resolve the diurnal cycle from two models (GFDL-CM3 and IPSL-CM5A-LR) (Fig. 3.3b,c).

Figs. 3.3d,e show T_{max} and $\mathrm{TW_{max}}$ trends for all locations normalized by the tropical mean warming under RCP 8.5. T_{max} warming is spatially inhomogeneous over land ranging from 1.0°C to 2.3°C for each 1°C of tropical mean warming (Fig. 3.3d) consistent with previous findings. In contrast, we find that increases of $\mathrm{TW_{max}}$ has no significant land-ocean contrast ranging from 0.8°C to 1.3°C for each 1°C of tropical mean warming (Fig. 3.3e). Using the annual-maximum 3-hourly TW for $\mathrm{TW_{max}}$ does not change this result.

The spatially uniform TW_{max} trend (Fig. 3.3e) is not a cancellation of errors among different models. Instead, all models show good agreement on TW_{max} trend, even down to regional scales. Fig. 3.4 shows the model spread (2.5-97.5th percentiles) of T_{max} and TW_{max} projections for four selected regions that have caught substantial attention in the literature, namely the Amazon rainforest, the Maritime Continent, the Indian peninsula, and the Sahel. Projected T_{max} warming has a large spread among models, which is especially prominent in the Amazon rainforest, consistent with earlier analysis (Vogel et al., 2017). However, for regional TW_{max}, all 22 climate models project a close to 1:1 ratio with the tropical mean warming. Using the annual maximum of 3-hourly TW does not change this result. Intriguingly, the model spread of T_{max} tends to grow with the amplitude of the projected warming (pronounced for the Amazon rainforest and the Maritime Continent), whereas the model spread of TW_{max} does not show evident growth within the range of simulated warming (roughly 4°C). That the inter-model spread is much less for TW_{max} projections than for T_{max} is also true for other tropical land regions.

To summarize, global climate models predict that TW_{max} will increase roughly uniformly in the tropics by about 1°C for each 1°C of tropical mean warming. Models show wide spread on regional T_{max} projections but agree very well upon regional TW_{max}.

Global climate models shown in Figs. 3.3, 3.4 are consistent with the theoretical consideration in Eq. 3.2-3.5. For each 1°C of tropical mean warming, models on average give 1.05 °C of $\Delta TW_{max,Land}$, 0.93°C of $\Delta TW_{max,Ocean}$, and 0.91°C of the warmest-quartile-mean SST increase, all close to 1°C.
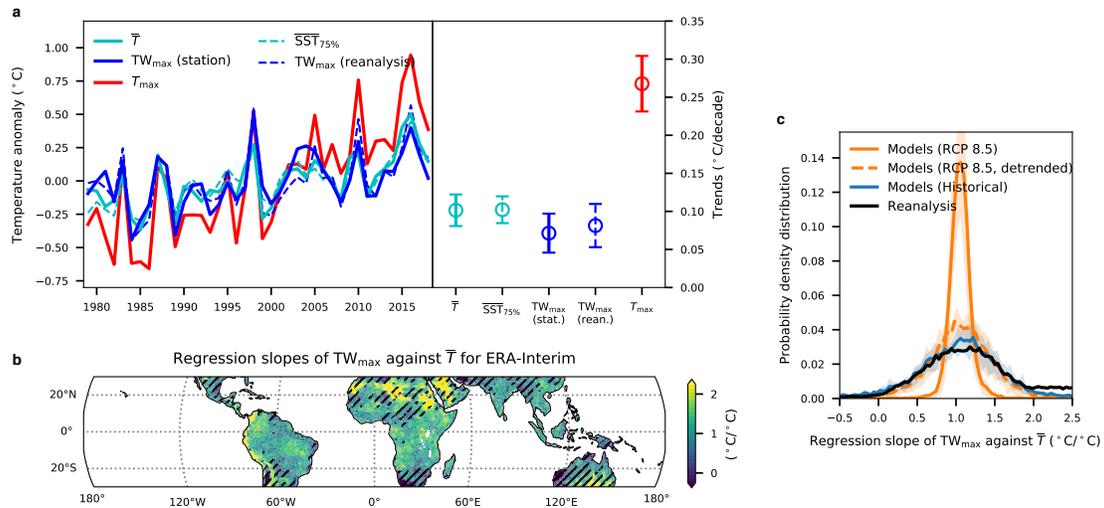
Figure 3.5: $\mathrm{TW_{max}}$ **in observations and reanalysis data. a**, Time series and corresponding linear trends of tropical mean temperature ($\overline{T}$; solid cyan), land-mean T_{max} (red), land-mean $\mathrm{TW_{max}}$ from stations (solid blue) and ERA-Interim (dashed blue), and the warmest-quartile-mean SST from HadISST (dashed cyan) for 1979-2018 (20°S-20°N). The confidence intervals for the linear trends represent 95% significance assuming that the detrended annual data points are independent. **b**, Linear regression slopes of local $\mathrm{TW_{max}}$ onto $\overline{T}$ in the interannual variabilities (linear trends removed) from ERA-Interim for 1979-2018. Regions where $\mathrm{TW_{max}}$ and $\overline{T}$ are not correlated on a 95% significance level are hatched. **c**. Histograms of regression slopes of local $\mathrm{TW_{max}}$ onto $\overline{T}$ (linear trends removed) for 1979-2005 in ERA-Interim (black solid) and models (blue solid), and for the global warming simulations in models (orange dashed). The same histogram for non-detrended global warming simulations (Fig. 3.3e) is also shown (orange solid). Shading indicates the 25-75th percentiles of models.

From 1979 to 2018, the tropical (20°S-20°N) land mean T_{max} trend has a 95% confidence interval of 0.24-0.31°C/decade, which is almost three times of the tropical mean warming of 0.08-0.12°C/decade based on ERA-Interim reanalysis (Dee et al., 2011) (Fig. 3.5a). TW_{max} has a trend of 0.05-0.10°C/decade, very similar to the tropical mean warming, and the interannual variabilities of the two are highly correlated with a correlation coefficient of 0.85 (Fig. 3.5a). Using the annual-maximum 3-hourly TW from ERA-Interim yields very similar anomalies, though the long-term trend is smaller. Furthermore, station measurements of TW provided by HadISD (Dunn et al., 2016) show that TW_{max} averaged over tropical stations are highly correlated with that from ERA-Interim and have a similar trend of 0.05-0.10°C/decade (Fig. 3.5a). The consistency of reanalysis data with station observations and the theory lends support to the quality of the reanalysis data over tropical land.

The warmest-quartile-mean SST (the average of the top 25% of monthly SST at all grid points within each year) from HadISST (Rayner et al., 2003) is highly correlated with land-mean TW_{max} and has a similar trend of 0.08-0.12°C/decade (Fig. 3.5a). Satellite SST observations and station TW observations are largely independent, and the very good consistency in their extreme values lends strong support to the aforementioned argument that TW_{max} over land is coupled to the warmest SSTs. Strong El Niño events have the potential of warming the warmest SSTs and, as a result, affect TW_{max} over land (e.g., 1998 in Fig. 3.5a).

Location-specific evaluation of long-term TW_{max} trends for the observations suffers

from the smallness of the warming signal, but interannual variability of SST provides room for testing the 1:1 relationship with TW_{max}. Regression slopes of TW_{max} (ERA-Interim) onto the tropical mean temperature (linear trends removed) is relatively uniform over most of the land regions within 20°S-20°N (Fig. 3.5b) with a mode value close to 1 (Fig. 3.5c). This relationship loosens in the subtropics (indicated by the hatching in Fig. 3.5b), consistent with the latitudinal range where the theory works (Zhang & Fueglistaler, 2020). That the Andes and the southern edge of the Sahara have much higher TW_{max} sensitivity does not violate the proposed theory, as climatological TW_{max} in those regions is too low to trigger convection and thus not constrained by the aforementioned mechanism. The standard deviation of these slopes in the reanalysis is larger than that for the global warming simulations shown in Fig. 3.3e (Fig. 3.5c). A likely explanation is that the spatial pattern of TW_{max} can change in the interannual variability and such a spatial rearrangement can cause a spread in the regression slopes but does not affect the tropical averages shown in Fig. 3.5a. Indeed, global climate models also show a similar spread of TW_{max} trends under historical radiative forcing, and the removal of long-term trends in the global warming simulations for the same set of models also result in a similar spread (Fig. 3.5c). Therefore, regional TW_{max} trends diagnosed from reanalysis data over the past 40 years are consistent with global climate models. Also for similar reasons, we do not expect every station to give the same TW_{max} trend either.

While we do not attempt to formulate an attribution statement for the TW_{max} trend over land seen in Fig. 3.5a, we note that the tight relationship in the overall trend, as well as higher frequency variability, strongly suggests that any attribution statements for the tropical mean temperature or SST can also be applied to TW_{max}.
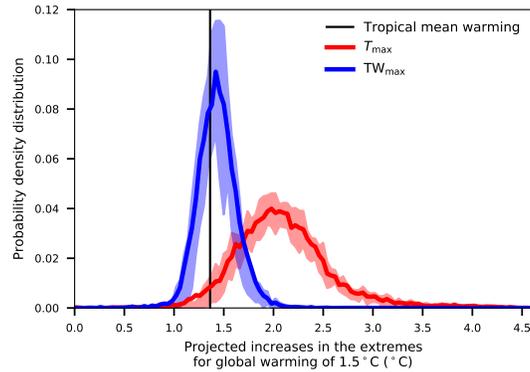
Figure 3.6: Uncertainty of T_{max} **and** $\mathrm{TW}_{\mathrm{max}}$ **projection in a 1.5°C warmer world (land between 20°S-20°N).** Distributions of model projected $\mathrm{TW}_{\mathrm{max}}$ increases (blue) and T_{max} increases (red) under RCP 8.5 at 1.5°C of global mean warming are shown. The distributions are constructed by linearly regressing local T_{max} and $\mathrm{TW}_{\mathrm{max}}$ increases onto global mean warming and taking the regression values at 1.5°C of global mean warming. Solid lines show the average distribution of all models and the shading indicates the 25-75th percentiles across models.

3.5   IMPLICATIONS FOR THE FUTURE CLIMATE

Consistency of model results with the theory and observations lends strong support to the capability of global climate models in properly simulating regional $\mathrm{TW}_{\mathrm{max}}$ increases. In a 1.5°C warmer world, the projected 66 per cent confidence interval (equivalent to IPCC's "likely range") for $\mathrm{TW}_{\mathrm{max}}$ increases across all tropical land regions (20°S-20°N) is 1.33-1.49°C, consistent with the simulated tropical mean warming of ∼1.4°C in a 1.5°C warmer climate (Fig. 3.6). On the other hand, projected T_{max} increases have a wider distribution, the absolute (relative) standard deviation of which is 3.7 (1.8) times of that of $\mathrm{TW}_{\mathrm{max}}$ increases. The reduction in uncertainty is more pronounced for regions where T_{max} projections are most uncertain. For example, in the Amazon rainforest and the Maritime Continent (Fig. 3.4), the absolute (relative) uncertainty of T_{max} increases is around 4 (2.5) times of that of $\mathrm{TW}_{\mathrm{max}}$ increases.

41

The non-local control of TW_{max} by the warmest SSTs seems to be at odds with the perception that these extreme events are driven by rare local meteorology, and this controversy deserves some clarification. While TW_{max} events are driven by local processes, the potential magnitude of TW_{max} is largely set by the uniform free tropospheric temperature. The effectiveness of this non-local control is evident in the uniformity of TW_{max} increases in Fig. 3.3d and the good agreement across models in Fig. 3.4, neither of which can be explained by the heterogeneity of local processes. Moreover, the existence of such a non-local control within the tropics also explains why the tropics are consistently warm and humid, but the highest TW and WBGT are observed in the subtropics (Willett & Sherwood, 2012; Pal & Eltahir, 2016; Im et al., 2017). These considerations thus support the picture that the magnitude of ΔTW_{max} across tropical land regions is set by the warmest SSTs and not local processes or the spatial pattern of SST.

Our results imply that curtailing global mean warming will have a proportional effect on regional TW_{max} in the tropics. The maximum 3-hourly TW (ERA-Interim) ever experienced in the past 40 years by 99.98% of the land area within 20°S-20°N is below 33 °C. Therefore, a 1.5°C or 2°C warmer world will likely exempt the majority of the tropical area from reaching the survival limit of 35°C. However, there exists little knowledge on safety thresholds for TW besides the survival limit (Sherwood, 2018), and 1°C of TW increase could have adverse health impact equivalent to that of several degrees of temperature increase. TW will thus have to be better calibrated to health impact before wider societal implementation. Nonetheless, the confidence in TW_{max} projection provided in this work still raises the confidence in projections of other calibrated heat stress metrics that accounts for TW, such as the WBGT.

4

Increasing Precipitation Inequality with

Warming

4.1 "Rich-get-richer"

Tropical precipitation falls very unevenly in space. Fig. 4.1a shows that three quarters of total precipitation falls on only a quarter of surface area when the observed monthly mean

precipitation intensities from Tropical precipitation Measuring Mission (TRMM) (Huffman et al., 2007) are sorted in ascending order. In the context of global warming, climate models predict enhancement of precipitation unevenness with increasing temperature (Giorgi et al., 2011; Liu & Allan, 2013; Lintner et al., 2012; Polson & Hegerl, 2017), which has implications for drought and flood projection and water resource management (Lintner et al., 2012). The unevenness of precipitation distribution is usually measured with the precipitation differences between the "wet" and the "dry" regions defined as, e.g., the upper portion and the lower portion of precipitation intensity (Allan et al., 2010; Liu & Allan, 2013; Gu & Adler, 2018; Polson et al., 2013; Polson & Hegerl, 2017), the local wettest and driest month of a year (Chou & Lan, 2012; Chou et al., 2013), the frequency of precipitation above and below some thresholds (Lintner et al., 2012). Despite the variety of metrics, the unevenness of precipitation is robustly projected to rise and this signal is emerging in the observational records (Liu & Allan, 2013; Polson & Hegerl, 2017; Allan et al., 2010; Chou & Lan, 2012; Gu & Adler, 2018).

Often cited in support of the strengthening contrast between wet and dry regions or seasons with global warming is the precipitation change mechanisms (e.g. Lintner et al., 2012) such as the "dry-get-drier, wet-get-wetter" mechanism (Held & Soden, 2006), the "upped-ante" mechanism (Neelin et al., 2003), or the "rich-get-richer" mechanism (Chou & Neelin, 2004). These mechanisms aim at explaining certain features of precipitation change which we will briefly summarize below, but none of them directly addresses the change in the unevenness. The mechanisms predicting future precipitation change usually make use of two approximations: (i) The relative humidity in the boundary-layer remains constant for energetic reasons (Held & Soden, 2000), so that the boundary-layer moisture

increases by 7%/K following the Clausius-Clapeyron relationship. (ii) The large-scale circulation pattern remains unchanged. The combination of these two approximations together with the assumption that changes in surface temperature gradients are small results in the amplification of moisture convergence or divergence by 7%/K with warming, leading to the amplification of the precipitation-minus-evaporation pattern by the same amount. This mechanism, widely known as "dry-get-drier, wet-get-wetter", accurately captures the climatological zonal-mean precipitation-minus-evaporation changes across all latitudes, yet its utility in explaining precipitation changes over land is limited for reasons discussed in Byrne & O'Gorman (2015). Another pair of mechanisms also result in the enhancement of contrast between wet and dry regions. The "upped-ante" mechanism predicts drying over marginally wet regions (Neelin et al., 2003). A warmer free troposphere raises the "ante" for convection and moisture in the wet regions will have to increase to maintain positive convective available potential energy (CAPE) while moisture in the dry regions is unable to increase by the same amount. The enhanced moisture gradients between wet and dry regions superimposed on the climatological advection from dry to wet regions thus cause negative moisture anomaly in between. The marginally convecting regions then fail to reach the "upped-ante" for convection and therefore dries with warming. At the same time, the "rich-get-richer" mechanism predicts a reduction in gross moist stability (GMS) due to increased boundary-layer moisture and thus enhances convection in the wet regions (Chou & Neelin, 2004), whereas tropospheric warming and deepening of convection may negate the effect of "rich-get-richer" mechanism in some cases (Chou et al., 2009).

Common to the previous mechanisms is the decomposition of precipitation changes into moisture changes and circulation changes (thermodynamic changes and dynamic

changes), as the longterm mean precipitation can be regarded as the large-scale circulation lifting and condensing the boundary-layer moisture. Such decomposition is also adapted in idealized models for tropical precipitation distribution (Pendergrass & Gerber, 2016). While the moisture changes (thermodynamic change) by 7%/K are robust in observations and climate models (Willett et al., 2007; Santer et al., 2007), in line with the aforementioned constant relative humidity assumption, the circulation changes have more significant uncertainty (Pfahl et al., 2017) especially on regional scales and relatively short monthly timescales (Chadwick et al., 2013; Byrne & O'Gorman, 2015), which precludes the aforementioned mechanisms from quantitatively explaining the robust increase in the unevenness of tropical precipitation.

In the following, we present a mechanism that does not assume unchanged circulations. We show that the unevenness of tropical precipitation is closely related to the frequency distribution of subcloud moist static energy (MSE) and that the changes in subcloud MSE distribution can be accurately captured by a simple scaling assuming constant relative humidity and uniform warming.

4.2 Overview of the mechanism in this work

A simple picture of the tropical atmosphere goes that tropical free tropospheric temperature is roughly uniform in the horizontal and follows a moist adiabat in the vertical which is determined by the subcloud MSE (see Eq. 1.2 for definition) in the convective regions (Bretherton & Smolarkiewicz, 1989; Emanuel et al., 1994). The rest of the tropics have lower subcloud MSE than the convective regions and are stable to deep convection. The unevenness of the tropical precipitation distribution should be related to the distribution

of subcloud MSE. Heuristically, if the subcloud MSE everywhere increases by the same amount, the unevenness of precipitation should be largely unchanged. On the other hand, if the highest subcloud MSEs for some reason increase faster than the rest, the free troposphere will warm up at a pace that the lower subcloud MSEs (in non-convective regions) cannot keep up with. Therefore dry regions will become more stably stratified and convection has to concentrate to wet regions with warming resulting in the increasing unevenness of precipitation. With global warming, the differential increase in MSE is a result of the nonlinearity of the Clausius-Clapeyron relationship meaning that saturation vapor pressures increase more for higher climatological temperatures, assuming uniform warming and relatively unchanged relative humidity. Since convective regions are generally warmer and contain more moisture than the non-convective regions, the same amount of warming will induce more increase in moisture in the wet regions than in the dry regions.

The above mechanism bears some similarity with the "upped-ante" mechanism but is essentially different in several ways. Firstly, although the "upped-ante" mechanism also recognizes the role of free tropospheric temperature in setting the convective "ante", the changes in free tropospheric temperature are externally determined: In the El Niño case it is due to teleconnection from neighboring Pacific, while in the global warming case it is due to absorption of infrared radiation (Neelin et al., 2003). Therefore the "upped-ante" mechanism is only able to address local precipitation changes but unable to tell whether a reduction in one place could be compensated by increase in another. Here we argue that free tropospheric temperature is endogenously determined by the highest subcloud MSE in the tropics rather than local factors or radiation. Therefore we are able to propose a closed theory for the distribution of precipitation within the entire tropics. Secondly, the "upped-
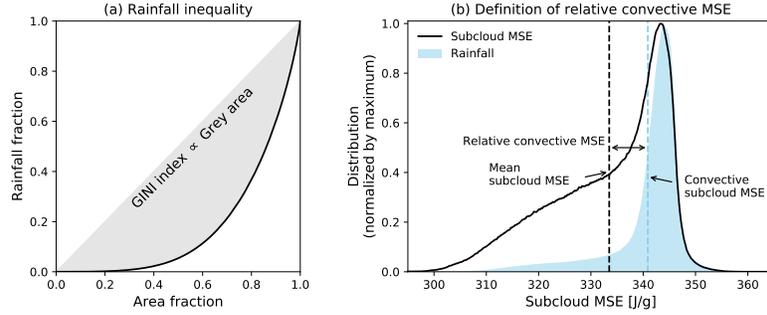
Figure 4.1: Schematics of the the Gini index and the relative convective MSE.

ante" mechanism also mentions increasing moisture gradients with warming, yet the reason

of which hinges on different moisture budgets in wet and dry regions. Here we give a gen-

eral explanation applying to both wet and dry regions making use of the assumption of

constant relative humidity.

4.3 METRICS OF UNEVENNESS

We use the Gini index, an economic index for inequality of income, as a single-value mea-

surement for the unevenness of precipitation distribution in space. Gini index has been

used by Rajah et al. (2014) to study the temporal distribution of precipitation before.

Monthly mean precipitation intensities between 30°S and 30°N are sorted in ascending

order then accumulated against area–This gives the same curve as in Fig. 1.2b. As illus-

trated in Fig. 4.1a, the Gini index is proportional to the area between the 1:1 line and the

cumulative precipitation fraction as a function of cumulative area fraction. The Gini index

ranges from 0 to 100, with 0 being completely even and 100 being extremely uneven. An

increase in the Gini index is an increase in the unevenness and is associated with a decrease

in the area of active convection. Compared to previous metrics for precipitation uneven-

ness that usually bisect the full distribution at arbitrary thresholds, the advantage of the Gini index is that it integrates the entire distribution of precipitation. Gini index does capture the enhanced contrast between wet and dry regions with warming as previous metrics do.

We use the relative convective MSE, the difference between the convective MSE and the tropical mean MSE, as a measurement of the shape of subcloud MSE distribution (Fig. 4.1(b)):

$$\text{Relative convective MSE} = \text{Convective subcloud MSE} - \text{Mean subcloud MSE}$$

$$(4.1)$$

Convective MSE is defined as the precipitation-weighted mean of subcloud MSE (see Eq. 1.3 for definition) treating precipitation as a proxy for convection intensity (Flannaghan et al., 2014). Since the atmosphere is only unstable to convection when subcloud MSE is high, the convective MSE is essentially a weighted mean of the highest subcloud MSE values. The relative convective MSE thus captures how close the entire distribution of tropical subcloud MSE is to convective instability.

4.4 Precipitation unevenness explained by relative convective MSE

4.4.1 Data

We first use observations and reanalysis to support the proposed mechanism then use global climate model simulations to understand future projections. precipitation observations from Tropical precipitation Measuring Mission (TRMM) (Huffman et al., 2007) on 0.25°x0.25° grid and Global Precipitation Climatology Project (GPCP) (Huffman

et al., 2001) on 1°x1° or 2.5°x2.5° grid and precipitation reanalysis from European Centre for Medium-Range Weather Forecasts reanalyses (ERA-Interim)(Dee et al., 2011) on 0.75°x0.75° grid are used. When matching a precipitation dataset to the subcloud MSE field based on ERA-Interim, the higher resolution dataset is interpolated to the grid of the lower resolution dataset conserving total flux for precipitation or bilinearly for MSE. For GPCP we only use data from the year 1988 on for data consistency. The microwave ocean measurements from the Special Sensor Microwave Imager (SSM/I) have been added to the blend of satellite infrared radiances and rain gauges since 1988. Inconsistency in the Gini index of tropical precipitation before and after 1988 is observed which is likely a result of adding new instruments. MSE is derived from monthly mean ERA-Interim reanalysis field and subcloud MSE is the average of MSE between 924.9 hPa and 1000.1 hPa following Williams et al. (2009); Williams & Pierrehumbert (2017). For the global warming simulations, we analyze monthly mean precipitation and diagnosed subcloud MSE from global climate models from the Coupled Model Intercomparison Project phase 5 (CMIP5) (Taylor et al., 2012) from the idealized CO_2 increase experiment (increasing CO_2 by 1% per year for 140 years until quadrupling). Simulations forced with emissions following the RCP 8.5 scenario yield similar results. To overcome the sparseness of output vertical levels in the subcloud layer (only 925 hPa and 1000 hPa) and lack of land information on 1000 hPa in most models, we calculated the subcloud MSE as the average of near-surface MSE and 925-hPa MSE.
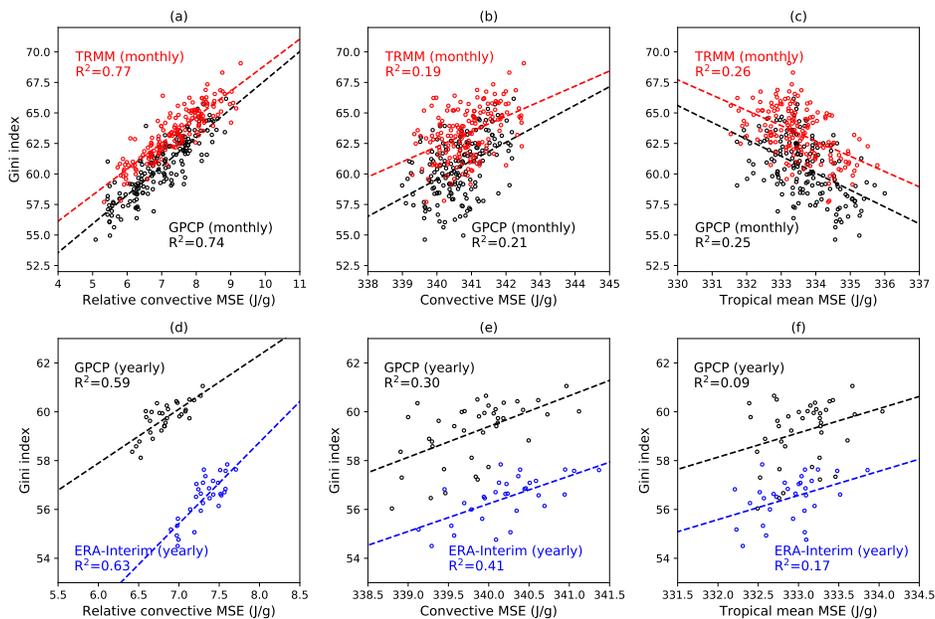
Figure 4.2: Gini index scattered against relative convective MSE, convective MSE, and tropical mean MSE. Each point in (a,b,c) is a month from January 2001 to December 2014. Each point in (d,e,f) is a year from 1988 to 2018.

4.4.2 Observations and reanalysis

In this section, we will show the correspondence between the relative convective MSE (convective MSE minus the tropical mean MSE) defined in the previous section and the Gini index of precipitation on multiple timescales in both observations/reanalysis and climate models. However, in the rest of the paper, we will focus on the yearly timescale to understand long-term trends.

In the observations and reanalysis data, the explained month-to-month variability is 77% for TRMM precipitation and 74% for GPCP precipitation for all months from 2001 to 2014 (Fig. 4.2a) and the explained interannual variability is 63% for ERA-Interim precipitation and 59% for GPCP precipitation from 1988 to 2018 (Fig. 4.2d). The explained

interannual variability in TRMM precipitation is only 32% (not shown) which could be a result of short record length. It is worth noticing that the monthly data shown in Fig. 4.2a are not deseasonalized. While this demonstrates that the proposed mechanism works for all seasons in general, there is the caveat that the high correlation is due to the strong seasonality of both two variables rather than any causality. However, the fact that the two components of relative convective MSE (convective MSE and the tropical mean MSE) are not correlated with the Gini index even though they exhibit strong seasonality (Fig. 4.2b, c) provides further support, and the same applies to the interannual variability (Fig. 4.2e, f). Therefore, the high correlation between the Gini index and the relative convective MSE shown in Fig. 4.2a and d is very likely a result of the mechanism proposed in Section 4.2. This tight relationship only emerges on timescale longer than a month, whereas on a daily timescale, the relationship is loosened by stochastic processes and the correlation coefficient is much less.

4.4.3 CMIP5 MODELS

In CMIP5 models, the tight relationship between the annual-mean Gini index and relative convective MSE also applies. The unevenness of precipitation increases in 26 out of the 28 models examined here, indicated by the increased Gini index by the end of the simulation. Relative convective MSE explains on average about 80% of variability in the annual-mean Gini index in all models (Fig. 4.3). The R^2 values for all models are shown in Table 4.1, where 21 out of 27 models has R^2 values of higher than 0.85, though 4 models show R^2 values of below 0.41. Up to this point, we can conclude that the robust increasing precipitation unevenness among models can be explained by the robust increase in relative convec-
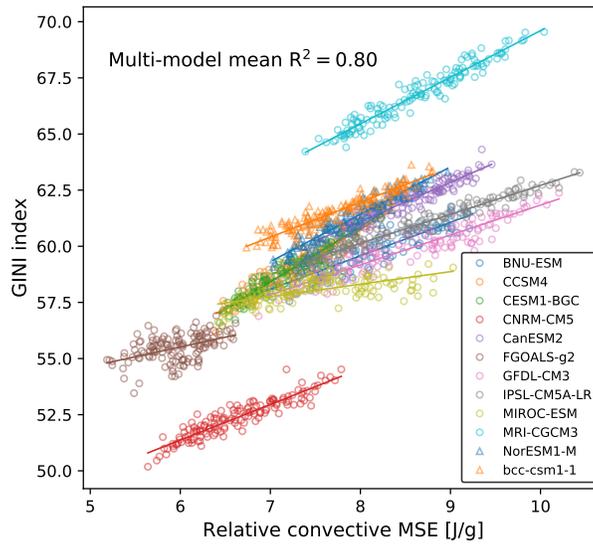
Figure 4.3: Gini index scattered against relative convective MSE of each CMIP5 model in the idealized CO$_2$ increase experiment. Each marker is a year. Selected models from different modeling centers are shown.

tive MSE, which is going to be understood with a simple scaling in the following section.

4.5   Increasing relative convective MSE due to Clausius-Clapeyron law

Fig. 4.4 shows the subcloud MSE distribution in the present climate (first 10 years of simulation) and a warmer climate (last 10 years of simulation) averaged over all models. In addition to a shift of the entire distribution to higher MSE values with warming, the shape of the distribution has also changed. The high end of the distribution has increased more in MSE than the low end, resulting in the broadening of the distribution in MSE space. Since the convective subcloud MSE is a weighted-mean of the highest subcloud MSE values (Fig. 4.1b), the relative convective MSE increases faster than the tropical mean with warming.

The change in the distribution of subcloud MSE can be explained by a uniform temperature increase. We predict the distribution in the last 10 years of the simulation by perturb-

Table 4.1: Modeled change in the Gini index of precipitation and relative convective MSE

#	Model	Δ (Gini index)	Δ (Relative convective MSE) (unit: J/g)	r^2
1	ACCESS1-0	3.50	2.34	0.91
2	ACCESS1-3	2.98	2.42	0.89
3	BNU-ESM	2.54	1.93	0.84
4	CCSM4	3.48	1.53	0.91
5	CESM1-BGC	3.36	1.43	0.93
6	CESM1-CAM5	2.98	1.80	0.92
7	CMCC-CM	5.14	2.96	0.96
8	CNRM-CM5	2.50	1.66	0.86
9	CNRM-CM5-2	2.42	1.70	0.86
10	CanESM2	2.36	1.45	0.88
11	FGOALS-g2	-0.38	0.75	0.23
12	FGOALS-s2	-0.36	1.24	0.04
13	GFDL-CM3	2.99	2.55	0.86
14	GFDL-ESM2G	1.97	1.80	0.78
15	GFDL-ESM2M	1.88	1.84	0.77
16	HadGEM2-ES	3.08	2.35	0.90
17	IPSL-CM5A-LR	3.53	2.76	0.96
18	IPSL-CM5A-MR	2.57	2.41	0.91
19	IPSL-CM5B-LR	2.02	1.97	0.85
20	MIROC-ESM	1.10	2.05	0.41
21	MIROC5	0.32	1.13	0.37
22	MPI-ESM-LR	5.40	3.15	0.96
23	MPI-ESM-MR	5.85	3.13	0.96
24	MPI-ESM-P	5.54	3.18	0.96
25	MRI-CGCM3	3.92	1.94	0.94
26	NorESM1-M	2.88	1.44	0.90
27	NorESM1-ME	3.07	1.54	0.88
28	bcc-csm1-1	2.60	1.69	0.89
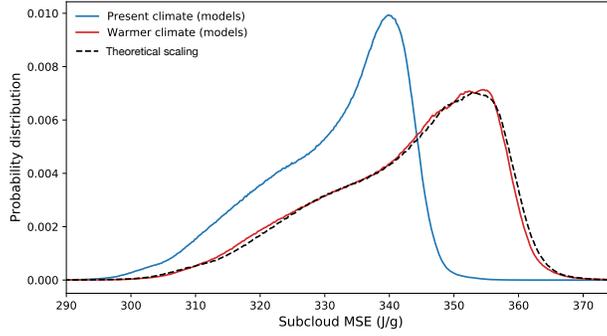
Figure 4.4: Multi-model-mean subcloud MSE distribution of subcloud MSE. The the first (solid blue) and last (solid red) 10 years of the simulation and the predicted distribution from perturbation of the first 10 years (dashed black line) are shown. The dashed gray line shows the effect of temperature change only.

ing the subcloud MSE in the first 10 years. For each location and month, subcloud MSE is perturbed by the amount Δh defined as follows:

$$\Delta h = c_p \Delta \overline{T} + L_v q \alpha \Delta \overline{T} \tag{4.2}$$

where $\Delta \overline{T}$ is the change in tropical mean temperature, $\alpha = 7\%$/K which is approximately the rate at which saturation vapor pressure increases with temperature according to the Clausius-Clapeyron relationship, and q is the specific humidity. The Δh prediction in Eq. (4.2) only uses local information for the specific humidity q and the tropical mean temperature change ($\Delta \overline{T}$). In a nutshell, this scaling assumes unchanged relative humidities with warming and uniform warming (The "uniform" here means a shift in temperature histogram which does not necessarily mean spatially uniform warming. A uniform shift in temperature histogram and a reshuffle of temperatures in space can result in spatially non-uniform warming).

Despite the crudeness, the scaling captures the shift and the shape change of subcloud
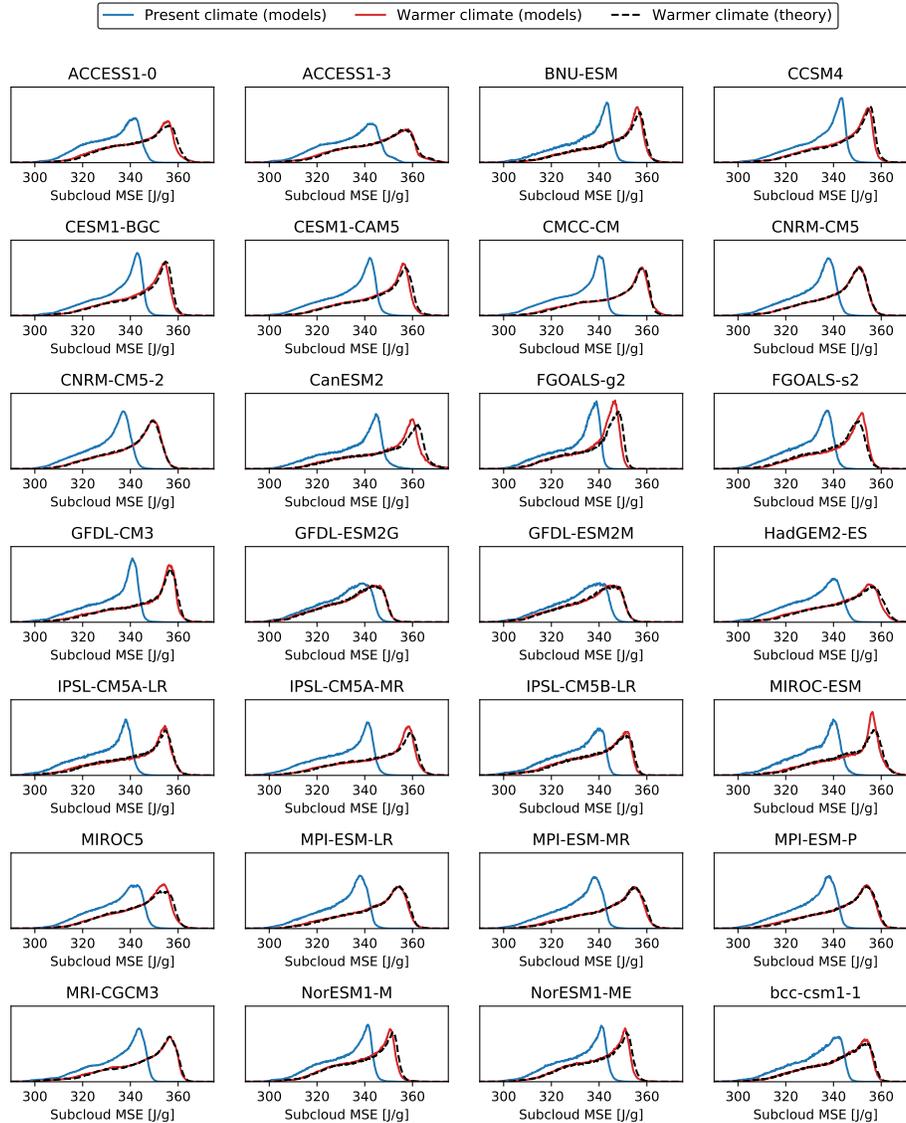
Figure 4.5: The shape change of subcloud MSE distribution is captured by the theoretical scaling. Subcloud MSE distribution in the first and last 10 years of the simulation and the predicted distribution from perturbation of the 10 years (dashed black lines) for each model. Labels of Y axis should be "probability distribution" as in Fig. 4.4 and are omitted here.
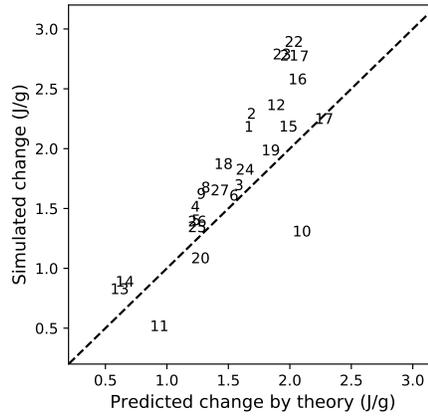
Figure 4.6: Simulated change in relative convective MSE for each model vs. the predicted change by theory. The corresponding model for each number is listed in Table 4.1

.

MSE very accurately not only in the multi-model mean (Fig. 4.4), but also in each model Fig. 4.5. The change in the relative convective MSE by the end of the simulation for each model can be predicted by the difference between moisture in the convective regions ($\widehat{q}$; precipitation-weighted moisture) and tropical mean moisture ($\overline{q}$) given the tropical mean warming ($\Delta\overline{T}$) by the end of the simulation following the Clausius-Clapeyron relation (combining Eq. 4.1 and Eq. 4.2):

$$\Delta(\text{Relative convective MSE}) = \alpha\Delta\overline{T}L_v(\widehat{q} - \overline{q}) \tag{4.3}$$

Fig. 4.6 shows that Eq. (4.3) captures the inter-model scatter of simulated changes in the relative convective MSE. Models with larger moisture gradients in the base state undergo larger relative convective MSE change. The predicted changes are somewhat biased which is not surprising given the simplicity of Eq. (4.2). Specifically, Eq. (4.2) does not take into

account that relative humidity tends to weakly increase over the ocean and decrease over the land (Boer, 1993) and the warming is not spatially uniform.

4.6 Conclusion

We have shown that the increasing unevenness of tropical precipitation with global warming can be understood as a result that the Clausius-Clapeyron relationship amplifying the moist static energy (MSE) gradients in the subcloud layer. There are two essential links in this chain of reasoning: (i) The unevenness of the monthly precipitation in both observations and models (measured by the Gini index) is well explained by the relative convective MSE which is a bulk metric of how high the highest subcloud MSE is compared to the tropical mean. (ii) The simulated change in relative convective MSE with global warming can be very well captured by subcloud MSE change associated with uniform warming and fixed relative humidity.

Our argument relates to the previously published concept of SST threshold for convection (Palmen, 1948), whereby the invariant shape of SST distribution with warming implies constant convective area since the SST threshold warms as much as the mean SST (Williams et al., 2009; Johnson & Xie, 2010). Our work stresses that even uniform SST warming leads to a decrease in convective area fraction as a consequence of the Clausius-Clapeyron scaling of subcloud MSE, irrespective of whatever changes in large-scale circulation may occur.

5

Linearity of outgoing longwave radiation

5.1 A MISSING LINK FROM AN ATMOSPHERIC COLUMN TO THE GLOBAL MEAN

A standard paradigm for analyzing the Earth's climate and climate sensitivity is to treat it

as a linear system (e.g. Gregory et al., 2004). An implicit assumption in those treatments

is that the global-mean outgoing longwave radiation (OLR) is linear with the global-mean

surface temperature ($\overline{T_s}$). Indeed, as is shown in Fig. 5.1a, the annual-mean global mean
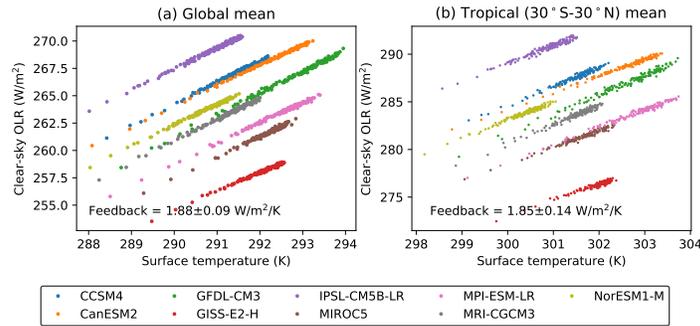
Figure 5.1: Clear-sky OLR vs. surface temperature of CMIP5 models abrupt 4xCO$_2$ experiment. (a) Annual-mean and global-mean OLR vs. surface temperature. (b) The same as (a) but for the tropical (30°S-30°N) mean.

clear-sky OLR ($\overline{\text{OLR}}$) from the Coupled Model Intercomparison Project phase 5 (CMIP5) (Taylor et al., 2012) increases in a strikingly linear fashion with $\overline{T_s}$ for each model after abruptly quadrupling CO$_2$ concentration. Though models warm by various amounts after 150 years, the longwave clear-sky (LWCS) feedback (slope of the linear regression of $\overline{\text{OLR}}$ against $\overline{T_s}$) varies by only 5% around the mean value of 1.88 W/m^2/K for the 9 models from different modeling centers shown, consistent with previous work (Andrews et al., 2015). Notably, this value is also consistent with the idealized single-column model calculation by Koll & Cronin (2018) over a wide range of surface temperatures.

This robust global mean LWCS feedback, however, is made up of non-uniform local responses which moreover differ amongst models. The OLR increase per unit warming in the deep tropics is relatively low, and sometimes even negative, an effect known as the "super-greenhouse effect". This phenomenon has received some attention as a local feedback (Raval & Ramanathan, 1989; Valero et al., 1997; Stephens & Greenwald, 1991; Stephens et al., 2016; Dewey & Goldblatt, 2018; Raghuraman et al., 2019), but its relevance for the global climate sensitivity is unclear given that other regions seem to emit more

OLR per unit warming to compensate. Here we would like to understand this compensation and whether it is guaranteed under global warming.

The origin of OLR being linear with T_s rather than quartic (as suggested by the Stefan–Boltzmann law) lies in the water vapor feedback given that the relative humidity (RH) remains constant with warming (Ingram, 2010; Koll & Cronin, 2018). OLR calculation for a single-column atmospheric model does confirm that there exists a wide range of T_s where the LWCS feedback varies by less than $\pm 10\%$ around 2.2 W/m^2/K if the atmospheric column follows a warming trajectory of constant RH (Koll & Cronin, 2018). Here we conceptually describe the behavior of this single-column atmospheric model with the following equation:

$$\left.\frac{\partial \mathrm{OLR}}{\partial T_s}\right|_{\mathrm{RH}} \approx \alpha \approx 2\,\mathrm{W/m^2/K} \tag{5.1}$$

However, unlike the idealized column model, the vertical profile of RH in realistic atmospheres is rarely uniform and inversions can complicate the vertical temperature profiles. Furthermore, the RH profile in a given column need not be constant, as previous studies have found that the geographical distribution of relative humidity is strongly affected by the atmospheric circulation which affects the local OLR-Ts relationship (Raval et al., 1994; Allan et al., 1999; Held & Soden, 2000). Therefore, Eq. 5.1 is not directly applicable to the global mean of CMIP5 models shown in Fig. 5.1a. Note that since Koll and Cronin (2018) motivated their theoretical and idealized modeling work with the observed joint distribution of local OLR vs. local T_s regardless of column RH, it has not been articulated how their results can be applied to the linearity of the global-mean OLR vs. the global-mean T_s. It is thus unclear whether the agreement between the global climate models and the idealized single-column model is coincidental.

Here we show that this agreement is not a coincidence. We first investigate the spatial patterns of LWCS feedback in CMIP5 models to get a sense of how the spatial patterns compensate and further show that the spatial patterns are tied to column RH changes. We find that α is independent of column RH so long as the column RH is interpreted as being in the free troposphere. We show analytically that the global mean LWCS feedback will be equal to α so long as the global histogram of column RH doesn't change with warming, a criterion satisfied to a large degree by all CMIP5 models.

5.2 Spatial pattern of LWCS feedback and connection to column RH

5.2.1 Materials and Methods

The LWCS feedback is diagnosed following the forcing-response analysis introduced by Gregory et al. (2004). The monthly mean output of global climate models from Coupled Model Intercomparison Project phase 5 (Taylor et al., 2012) for the abrupt 4xCO$_2$ experiment (abruptly quadrupling CO$_2$ then integrate for 150 years) is analyzed. The local long-wave clear-sky feedback is determined by linear regression of local clear-sky OLR onto *local* surface temperature to emphasize the physical connection between OLR and local surface temperature (The advantage of using locally defined feedback is discussed in Feldl & Roe (2013)), which is not the same as earlier work that regresses local radiative quantities onto global mean surface temperature (e.g. Andrews et al., 2015; Stephens et al., 2016). As the clear-sky feedback is roughly constant throughout the entire length of the simulation (150 years; Fig. 5.1), we will not separate the fast response epoch ($\sim$ the first 20 years) and the slow response epoch (the rest 130 years or so) in the following analysis.

Column relative humidity is calculated as the water vapor mass divided by the saturated

water vapor mass within the column. To calculate the water vapor mass between every two pressure levels, specific humidity data are interpolated to the center of pressure levels assuming linearity with the logarithm of pressure, and then weighted by the pressure difference. The upper boundary for column RH calculation is chosen to be 300 hPa. Ideally, the tropopause is the upper boundary for the column, but considering the limited output levels of CMIP5 models, this choice is made to include as much of the tropospheric water vapor as possible on condition of not including the stratosphere. This is because neglecting the water vapor between 300 hPa and the tropopause makes little difference to column RH due to very low temperature there, while contamination from the stratosphere can bias the saturated water vapor a column can hold due to the inversion.

5.2.2   Results

We demonstrate the spatial pattern of the LWCS feedback and the ensuing compensation which produces the robust value of α shown in Fig. 5.1a by gradually increasing the spatial dimensions of our analysis. Fig. 5.2a shows the zonal-mean feedback obtained by regressing the zonal-mean clear-sky OLR onto the zonal-mean surface temperature using decadal mean data (to smooth over inter-annual internal variability). The zonal-mean LWCS feedback is not uniform across latitudes, with a minimum of 1 W/m^2/K in the deep tropics and a typical value of 2 W/m^2/K in the extratropics in the multi-model mean. The linearity of clear-sky OLR with T_s can be assessed by the R^2 of the local OLR-T_s linear regression. The linearity is remarkably strong in the extratropics, indicated by close to 100% of explained variance (Fig. 5.2b), and somewhat weaker in the tropics. Models also tend to agree better in the extratropics as measured by the standard deviation of LWCS feedback (Fig. 5.2c).
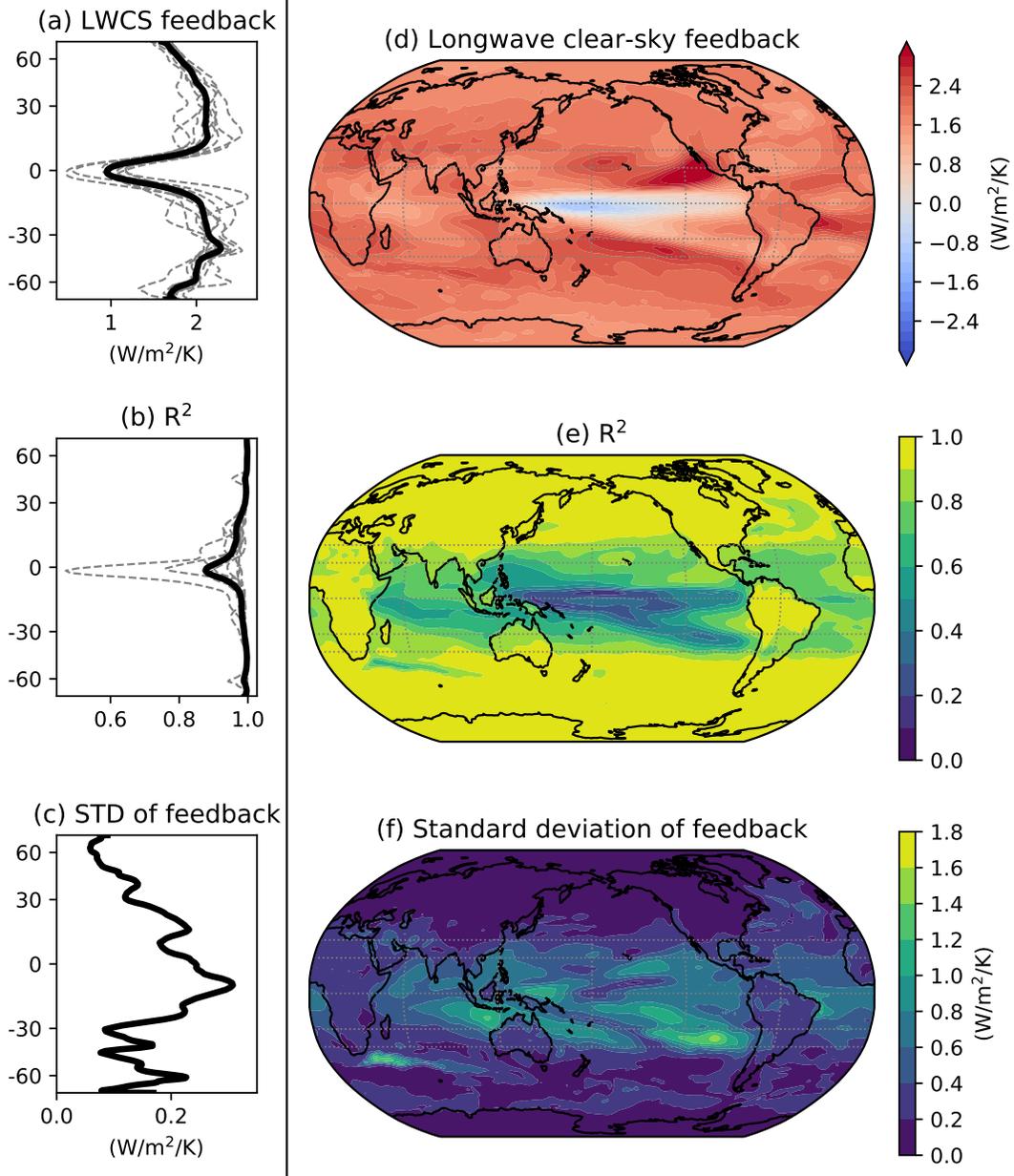
Figure 5.2: Spatial patterns of LWCS feedback in CMIP5 models. (a) Zonal-mean LWCS feedback for each model (dashed) and the multi-model mean (solid). (b) The R^2 of the linear regression of zonal-mean OLR onto the zonal-mean T_s for each model (dashed) and the multi-model mean (solid). (c) Standard deviation of the zonal-mean LWCS feedback among models. (d), (e), and (f) show the same variables as in (a), (b), and (c) respectively on 2D maps.
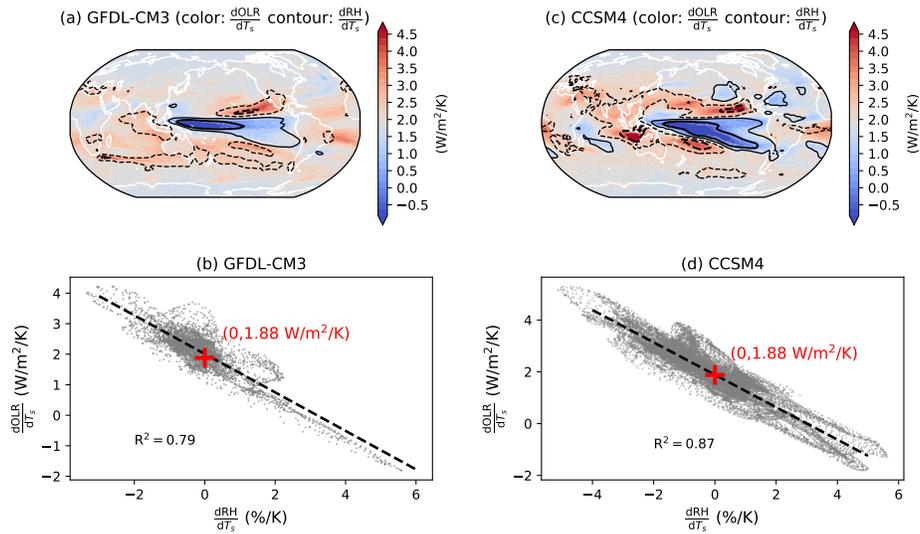
Figure 5.3: Spatial pattern of LWCS feedback and relative humidity changes. (a) Location-specific longwave clear-sky feedback parameters (color shading) and the sensitivity of column relative humidity (RH) to surface temperature (black contours) for GFDL-CM3. Contours of -3%/K (thick dashed), -1%/K (thin dashed), 1%/K (thin solid), 3%/K (thick solid) are shown. (b) Scatter plot of the two fields shown in (a) and the linear regression line. The red cross marks the point of zero column RH change and a LWCS feedback of 1.88 W/m^2/K. (c) and (d) are the same as (a) and (b) but for CCSM4.

Fig. 5.2d shows the map of LWCS feedback. In the extratropics, similar to the zonal mean (Fig. 5.2a), the LWCS feedback is relatively spatially uniform and lacks any land-ocean contrast. In the tropics, however, regions of negative feedback emerge, which is the "super-greenhouse effect" referred to in the Introduction. The linearity is again remarkably strong in the extratropics for each location but is weak within the 30°S-30°N latitude band (Fig. 5.2e). Models show very good agreement of the LWCS feedback in the extratropics, while in the tropics the standard deviation across models is of the same magnitude as the feedback itself (Fig. 5.2f), consistent with previous findings that models disagree on the locations and strengths of "super-greenhouse effect" (Stephens et al., 2016).

To understand the spatial pattern and the model spread of the LWCS feedback shown

in Fig. 5.2, we consider the joint dependence of OLR on T_s and RH. Invoking Eq. 5.1 but also allowing for RH changes with warming yields

$$\frac{\mathrm{dOLR}}{\mathrm{d}T_s} = \alpha + \beta \frac{\mathrm{dRH}}{\mathrm{d}T_s}, \tag{5.2}$$

where $\beta = \left. \frac{\partial \mathrm{OLR}}{\partial \mathrm{RH}} \right|_{T_s}$. Eq. 5.2 indicates that the spatial pattern of the LWCS feedback should be closely related to the spatial pattern of $\frac{\mathrm{dRH}}{\mathrm{d}T_s}$. A similar idea is mentioned in Held & Soden (2000). In testing this idea, we begin by using column RH and later refine this by using the free tropospheric column RH.

Fig. 5.3 illustrates the accuracy of Eq. 5.2 with two models that feature different patterns of LWCS feedback. In GFDL-CM3 the regions of the super-greenhouse effect are mainly located on the equator in the western basin of the Pacific, while in CCSM4 these regions expand off the equator and are mainly located in the central Pacific. For both models, the spatial patterns of LWCS feedback (color shading) and the column RH changes (contours) are almost identical (Fig. 5.3a and c). To make this more explicit, we plot $\frac{\mathrm{dOLR}}{\mathrm{d}T_s}$ vs. $\frac{\mathrm{dRH}}{\mathrm{d}T_s}$ in Fig. 5.3b and d, taking only grid points within 30°S-30°N. The correlations for GFDL-CM3 and CCSM4 are -0.89 and -0.93 respectively, and -0.87 for all the 9 CMIP5 models in Fig. 5.1 on average. Moreover, the intercept of the linear regression is on average 1.9 W/m^2/K which indeed recovers the value of α (see Fig. 5.3b and d for GFDL-CM3 and CCSM4). In other words, for locations where column RH doesn't change with warming, the LWCS feedback is close to the value given by the single atmospheric column model.

A key feature of Fig. 5.3 a and c is that column RH increases in the deep tropics are accompanied by column RH decreases in the subtropics. This implies that the local effects of RH changes on OLR might cancel out in the global mean, or even just in the tropical mean

as indeed seen in Fig. 5.1b. This suggests that the robustness of the global mean LWCS feedback evident in Fig. 5.1 results from a geographical *rearrangement* of column RH values, without any change in the column RH histogram. We test these ideas in Section 5, but first, we return to the question to what extent Eq. 5.1 applies to realistic atmospheres with non-uniform RH profiles.

5.3 OLR-T_s relationship conditioned upon column RH

Eq. 5.1, a central result of (Koll & Cronin, 2018), was tested in an idealized single-column atmospheric model with vertically uniform RH profiles and moist adiabatic temperature profiles. However, we know that the real atmosphere exhibits more complicated vertical structures of temperature and RH which influence the OLR (Shine & Sinha, 1991; Huang et al., 2007).

To test the applicability of Eq. 5.1 to more realistic atmospheres, Fig. 5.4(a) shows the OLR dependence on T_s conditioned upon various column RH ranging from 40% to 70%. As expected, the OLR increases as column RH decreases for a given T_s. Furthermore, at relatively low T_s, the slope (the LWCS feedback) is around 1.9 W/m²/K for all column RH values, consistent with Eq. 5.1. However, OLR decreases with T_s at T_s above 303 K, which is inconsistent with Eq. 5.1. Although a flattening of the OLR-T_s curve is expected from the closing of the water vapor window (Koll & Cronin, 2018), this happens at a much higher temperature and cannot explain the *decreases* of OLR with T_s seen here. This decrease of OLR with T_s is distinct from the super-greenhouse effect discussed above because here it occurs even at fixed column RH.

What then causes this breakdown of Eq. 5.1 in realistic atmospheric columns? A single
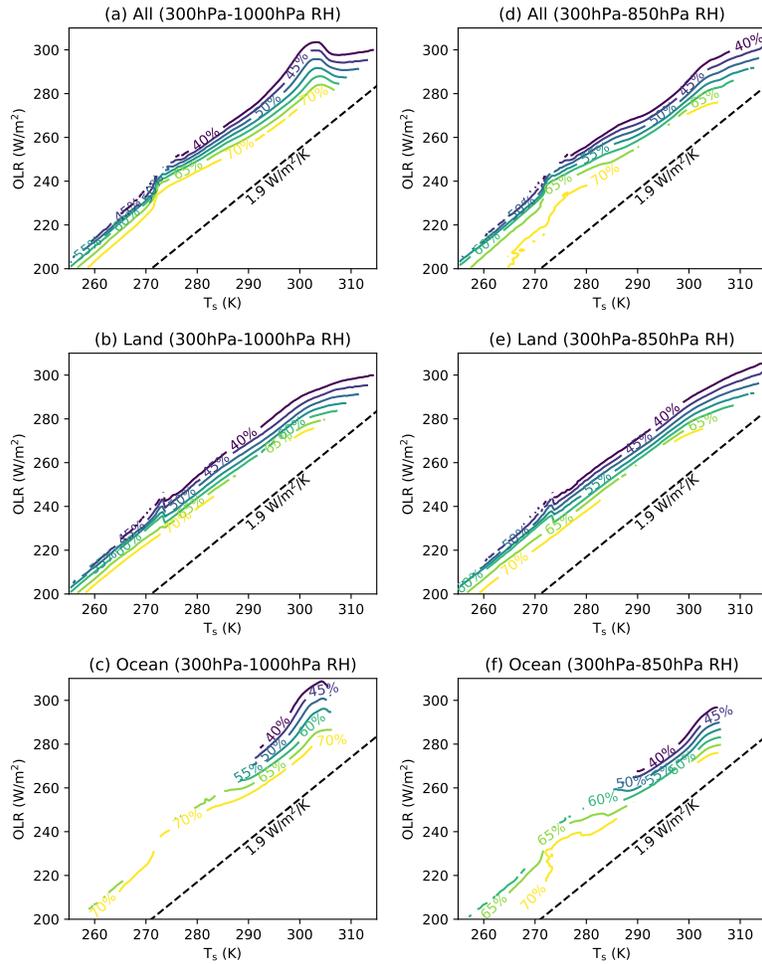
Figure 5.4: Clear-sky OLR vs. surface temperature conditioned upon various column RH values. Data from 9 CMIP5 models are included in the statistics. Column RH for 300 hPa-1000 hPa is used for (a), (b), (c) and column RH for 300 hPa-850 hPa (free troposphere) is used for (d), (e), (f). (a) and (d) include both land and ocean data, while (b) and (e) include land only, and (c) and (f) include ocean only. The dashed black line indicates a reference slope of $1.9 \, \text{W/m}^2/\text{K}$.

column RH is insufficient for representing the vertical structure of the water vapor in real-istic climate models, as the boundary-layer RH (Held & Soden, 2000; Byrne & O'Gorman, 2016) and the free tropospheric RH (Pierrehumbert, 1998; Pierrehumbert & Roca, 1998; Galewsky et al., 2005; Romps, 2014) are determined by essentially independent processes which are sometimes decoupled. Furthermore, it is known that in contrast to the upper troposphere, the influence of the boundary-layer RH on OLR is quite weak (Soden & Held, 2006; Soden et al., 2008). Physically this is because the boundary-layer air temper-ature is close to T_s and an increase in the emission from the boundary-layer water vapor is approximately equal to the decrease in surface emission. To strengthen this point, we con-duct experiments with PyRADS, a line-by-line radiation code, of varying free-tropospheric and boundary-layer RH separately under fixed T_s at 288 K (roughly equal to the present-day global mean temperature). We find that even though the total water vapor path above 850 hPa is only 1.4 times of that below 850 hPa, the OLR responses of the former are 17 times of that of the latter. This suggests that we should focus on free-tropospheric RH rather than boundary-layer RH. Fig. 5.4d shows the same OLR-T_s relationship as in Fig. 5.4a but now conditioned on the free-tropospheric (300 hPa-850 hPa) column RH. With this RH variable, the decrease in OLR with T_s at higher T_s disappears, and Eq. 5.1 applies for most RH and T_s values.

Returning to the decrease of OLR with T_s at high T_s as shown in Fig. 5.4a, we find that this decrease is caused by the transition from the lower T_s values populated by ocean regions to those higher T_s values populated by land regions. At fixed column RH, the boundary layer is dryer and the free troposphere is moister over land than over the ocean. Thus, as one transitions from ocean to land columns at fixed column RH, one swaps boundary-

layer moisture for free-tropospheric moisture which reduces the OLR, leading to the kink in Fig. 5.4a at roughly 303 K. Indeed, land alone has a more linear OLR-T_s relationship (Fig. 5.4(b)), though a mild decrease of OLR with T_s still exists for the warmest oceans (Fig. 5.4(c)) located in between the subtropical deserts (e.g., the Red Sea) over which the boundary layer is very dry and more "land-like". Note that this decrease of OLR with T_s conditioned upon column RH is not the same as the super-greenhouse effect over tropical oceans which is primarily the effect of changing RH as discussed in the previous section. Using free-tropospheric column RH, the land-ocean contrast is significantly reduced (Fig. 5.4e and f) and the OLR-T_s relationship over land is an extension that over the ocean to higher T_s.

To summarize, despite the diversity of RH and temperature profiles in realistic climate models, the LWCS feedback (α) is indeed independent of both T_s and RH consistent with Eq. 5.1 so long as RH is interpreted as free-tropospheric column RH. Therefore, Eq. 5.1 seems applicable to realistic atmospheres and we can turn to the additional condition on column RH distribution.

5.4   CONDITION FOR ROBUST GLOBAL-MEAN LWCS FEEDBACK

Now we answer the question under what conditions the compensation of local LWCS feedback seen in Section 3 is guaranteed to produce a global-mean LWCS feedback around 2 W/m^2/K, consistent with Eq. 5.1. In particular, we show that a sufficient condition is that the free-tropospheric column RH distribution, denoted as $F(\text{RH})$, stays invariant with global warming.

We denote the joint distribution of T_s and column RH as $f(T_s, \text{RH})$ whose integral in

T_s gives $F(\mathrm{RH})$. For convenience, we express the OLR in the following functional form which is equivalent to Eq. 5.1:

$$\mathrm{OLR}(T_s, \mathrm{RH}) = \alpha T_s + R(\mathrm{RH}), \tag{5.3}$$

where the specific functional form of $R(\mathrm{RH})$ is not of concern here. The global-mean clear-sky OLR $(\overline{\mathrm{OLR}})$ is thus

$$\begin{aligned}
\overline{\mathrm{OLR}} &= \int \mathrm{dRH} \int \mathrm{d}T_s f(T_s, \mathrm{RH}) \mathrm{OLR}(T_s, \mathrm{RH}) \tag{5.4}\\
&= \alpha \int \mathrm{dRH} \int \mathrm{d}T_s f(T_s, \mathrm{RH}) T_s + \int \mathrm{dRH} R(\mathrm{RH}) \int \mathrm{d}T_s f(T_s, \mathrm{RH}). \tag{5.5}
\end{aligned}$$

The integral in the first term of Eq. 5.5 gives the global mean surface temperature $(\overline{T_s})$ and the integral over T_s in the second term gives the column RH distribution, therefore

$$\overline{\mathrm{OLR}} = \alpha \overline{T_s} + \int \mathrm{dRH} R(\mathrm{RH}) F(\mathrm{RH}), \tag{5.6}$$

and thus

$$\delta\overline{\mathrm{OLR}} = \alpha \delta\overline{T_s} + \int \mathrm{dRH} R(\mathrm{RH}) \delta F(\mathrm{RH}). \tag{5.7}$$

If the column RH distribution remains constant with global warming, i.e.,

$$\delta F(\mathrm{RH}) \equiv 0, \tag{5.8}$$
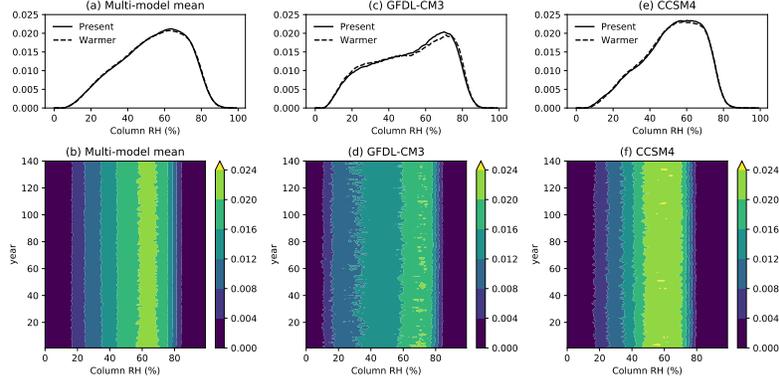
Figure 5.5: The invariant column RH histograms in CMIP5 models with warming. (a) The multi-model-mean histogram of free-tropospheric column RH in the first 10 years (solid; labeled "present") and the last 10 years (dashed; labeled "warmer") of the simulation. (b) Time series of the multi-model-mean free-tropospheric RH histogram throughout the simulation. (c) The same as (a) but for GFDL-CM3. (d) The same as (b) but for GFDL-CM3. (e) The same as (a) but for CCSM4. (f) The same as (b) but for CCSM4.

then we have

$$\frac{\delta \overline{\mathrm{OLR}}}{\delta \overline{T_s}} = \alpha. \tag{5.9}$$

Therefore, the global-mean LWCS feedback is equal to the constant-RH value α (Eq. 5.1),

Fig. 5.4) so long as the global column RH histogram is invariant under global warming.

Eq. 5.9 is thus the global-mean analog for Eq. 5.1, and Eq. 5.8 is the global analog for the

fixed-RH condition in the single-column model.

   This additional condition, described by Eq. 5.8, is indeed satisfied in CMIP5 models.

Fig. 5.5a shows that the multi-model mean histogram of free-tropospheric column RH is

largely unchanged between the first and the last 10 years of the simulation, and the same

is true for individual models (see Fig. 5.5c and Fig. 5.5e for GFDL-CM3 and CCSM4 as

examples). Furthermore, this invariance holds on a year-to-year basis (Fig. 5.5b, d, and f)

which guarantees the linearity of the global-mean OLR vs. global-mean T_s for annual mean

data as shown in Fig. 5.1. This result is consistent with previous work that finds that the free tropospheric RH is overwhelmingly controlled by the large-scale circulation (Pierrehumbert & Roca, 1998; Galewsky et al., 2005; Sherwood & Meyer, 2006), and constant free-tropospheric RH has long been proved to be an accurate leading order assumption with global warming (Manabe & Wetherald, 1975). Note that these results are also true if boundary-layer RH is included in the column RH calculation.

5.5 SUMMARY

This paper aims to connect the idealized model results of (Koll & Cronin, 2018) to the behavior of comprehensive climate models, in line with the hierarchical approach to climate science (Held, 2005; Jeevanjee et al., 2017; Maher et al., 2019). In particular, we sought to understand whether the robustness of LWCS feedback in CMIP5 models could be traced back to the single-column physics of (Koll & Cronin, 2018). We found that indeed it could, on the condition that the global free-tropospheric column RH histogram remains invariant under warming. This invariance of the global RH histogram is a global analog of the fixed-RH condition for single-column models. In this sense, we have shown that "fixed RH" is a good approximation for the atmosphere under global warming, and the linearity of global-mean OLR is a direct consequence of this.

This invariance of the global column RH histogram is manifest in Fig. 5.2a and c where a moistening of the deep tropics is accompanied by the drying of the subtropics. The super-greenhouse effect discussed in the Introduction arises when this deep-tropical moistening is strong enough to make $\frac{\mathrm{dOLR}}{\mathrm{d}T_s}$ negative (see Eq. 5.2). However, our results show that any such negative $\frac{\mathrm{dOLR}}{\mathrm{d}T_s}$ values must be offset elsewhere by anomalously positive values. This

means that, in a global or even a tropical-mean context, the clear-sky super-greenhouse effect is constrained to disappear (as evident in Fig. 5.1) and thus has little impact on large-scale climate.

-1

Summary and Outlook

A lot of studies in our field use maps as the backdrop of figures. As a result, maps have become the backdrop of thinking and understanding. However, this fixed-in-space perspective sometimes introduces unnecessary complexity and even confusion – The super-greenhouse effect in the previous chapter is one example. In this dissertation, we take a less worn path to understand the tropical climate, that is to emphasize probability distributions

rather than geographical locations. We expect the warmest SSTs and the highest subcloud MSEs to determine the free-tropospheric temperature profile no matter where they are located. The average subcloud MSE during times of deep convection is roughly the same regardless of location and land-ocean contrast. The annual-maximum wet-bulb temperatures over land respond to the magnitude of the warmest SSTs which are not fixed in space due to ENSO oscillation. The Gini index of precipitation can be captured by a simple metric of the highest subcloud MSEs relative to the tropical mean. The super-green house effect over tropical oceans is simply due to the spatial movement of convective centers and the positive correlation between convective activity and SST. These results exemplify the gain of deemphasizing the geographical location.

This dissertation's work could be further developed in many ways. One next step is to investigate the interplay of subcloud MSE distribution, the Gini index of precipitation, and the longwave and shortwave cloud radiative effect. There are also unanswered questions regarding the uniform convective MSE in Chapter 2: What determines the latitudinal range of the uniformity and how it is related to the lack of seasonality of the warmest SSTs shown in Chapter 1. There is also a question of the control of extratropical heat stress. I expect to see future research on those open questions.

References

Allan, R. P., Shine, K. P., Slingo, A., & Pamment, J. (1999). The dependence of clear-sky outgoing long-wave radiation on surface temperature and relative humidity. *Quarterly Journal of the Royal Meteorological Society*, 125(558), 2103–2126.

Allan, R. P., Soden, B. J., John, V. O., Ingram, W., & Good, P. (2010). Current changes in tropical precipitation. *Environmental Research Letters*, 5(2), 025205.

Andrews, T., Gregory, J. M., & Webb, M. J. (2015). The dependence of radiative forcing and feedback on evolving patterns of surface temperature change in climate models. *Journal of Climate*, 28(4), 1630–1648.

Arakawa, A. & Schubert, W. H. (1974). Interaction of a cumulus cloud ensemble with the large-scale environment, part i. *J. Atmos. Sci.*, 31(3), 674–701.

Back, L. & Bretherton, C. (2009). On the relationship between sst gradients, boundary layer winds, and convergence over the tropical oceans. *J. Climate*, 22, 4182–4196.

Betts, A. K. (1986). A new convective adjustment scheme. part i: Observational and theoretical basis. *Q. J. R. Meteorol. Soc.*, 112(473), 677–691.

Boer, G. J. (1993). Climate change and the regulation of the surface moisture and energy budgets. *Clim. Dynam.*, 8(5), 225–239.

Boos, W. & Kuang, Z. (2010). Dominant control of the south asian monsoon by orographic insulation versus plateau heating. *Nature*, 463, 218–222.

Bretherton, C. S. & Smolarkiewicz, P. K. (1989). Gravity waves, compensating subsidence and detrainment around cumulus clouds. *J. Atmos. Sci.*, 46(6), 740–759.

Brown, R. G. & Zhang, C. (1997). Variability of midtropospheric moisture and its effect on cloud-top height distribution during toga coare. *J. Atmos. Sci.*, 54(23), 2760–2774.

Byrne, M. P. & O'Gorman, P. A. (2013a). Land–ocean warming contrast over a wide range of climates: Convective quasi-equilibrium theory and idealized simulations. *Journal of Climate*, 26(12), 4000–4016.

Byrne, M. P. & O'Gorman, P. A. (2013b). Link between land-ocean warming contrast and surface relative humidities in simulations with coupled climate models. *Geophysical Research Letters*, 40(19), 5223–5227.

Byrne, M. P. & O'Gorman, P. A. (2015). The response of precipitation minus evapotranspiration to climate warming: Why the "wet-get-wetter, dry-get-drier" scaling does not hold over land. *Journal of Climate*, 28(20), 8078–8092.

Byrne, M. P. & O'Gorman, P. A. (2016). Understanding decreases in land relative humidity with global warming: Conceptual model and gcm simulations. *J. Climate*, 29(24), 9045–9061.

Byrne, M. P. & O'Gorman, P. A. (2018). Trends in continental temperature and humidity directly linked to ocean warming. *Proceedings of the National Academy of Sciences*, 115(19), 4863–4868.

Chadwick, R., Boutle, I., & Martin, G. (2013). Spatial patterns of precipitation change in cmip5: Why the rich do not get richer in the tropics. *Journal of Climate*, 26(11), 3803–3822.

Charney, J. (1963). A note on large-scale motions in the tropics. *J. Atmos. Sci.*, 20, 607–609.

Chou, C., Chiang, J. C., Lan, C.-W., Chung, C.-H., Liao, Y.-C., & Lee, C.-J. (2013). Increase in the range between wet and dry season precipitation. *Nature Geoscience*, 6(4), 263.

Chou, C. & Lan, C.-W. (2012). Changes in the annual range of precipitation under global warming. *Journal of Climate*, 25(1), 222–235.

Chou, C. & Neelin, J. D. (2004). Mechanisms of global warming impacts on regional tropical precipitation. *Journal of climate*, 17(13), 2688–2701.

Chou, C., Neelin, J. D., Chen, C.-A., & Tu, J.-Y. (2009). Evaluating the "rich-get-richer" mechanism in tropical precipitation change under global warming. *Journal of Climate*, 22(8), 1982–2005.

Coffel, E. D., Horton, R. M., Winter, J. M., & Mankin, J. S. (2019). Nonlinear increases in extreme temperatures paradoxically dampen increases in extreme humid-heat. *Environmental Research Letters*, 14(8), 084003.

Dee, D. P., Uppala, S., Simmons, A., Berrisford, P., Poli, P., Kobayashi, S., Andrae, U., Balmaseda, M., Balsamo, G., Bauer, d. P., et al. (2011). The era-interim reanalysis: Configuration and performance of the data assimilation system. *Quarterly Journal of the royal meteorological society*, 137(656), 553–597.

Delworth, T. L., Mahlman, J., & Knutson, T. R. (1999). Changes in heat index associated with co2-induced global warming. *Climatic Change*, 43(2), 369–386.

Dewey, M. & Goldblatt, C. (2018). Evidence for radiative-convective bistability in tropical atmospheres. *Geophysical Research Letters*, 45(19), 10–673.

Dunn, R. J., Willett, K. M., Parker, D. E., & Mitchell, L. (2016). Expanding hadisd: quality-controlled, sub-daily station data from 1931. *Geoscientific Instrumentation, Methods and Data Systems*, 5(2), 473–491.

Emanuel, K. (2007). Quasi-equilibrium dynamics of the tropical atmosphere. *The Global Circulation of the Atmosphere*, (pp. 186–218).

Emanuel, K. (2019). Inferences from simple models of slow, convectively coupled processes. *J. Atmos. Sci.*, 76(1), 195–208.

Emanuel, K., Neelin, J., & Bretherton, C. (1994). On large-scale circulations in convecting atmospheres. *Q. J. R. Meteorol. Soc.*, 120(519), 1111–2157.

Feldl, N. & Roe, G. (2013). Four perspectives on climate feedbacks. *Geophysical Research Letters*, 40(15), 4007–4011.

Fischer, E. M. & Knutti, R. (2013). Robust projections of combined humidity and temperature extremes. *Nature Climate Change*, 3(2), 126.

Flannaghan, T. J., Fueglistaler, S., Held, I. M., Po-Chedley, S., Wyman, B., & Zhao, M. (2014). Tropical temperature trends in Atmospheric General Circulation Model simulations and the impact of uncertainties in observed SSTs. *J. Geophys. Res.*, 119(23), 13,327–13,337.

Funatsu, B. & Waugh, D. (2008). Connections between potential vorticity intrusions and convection in the eastern tropical pacific. *J. Atmos. Sci.*, 65, 987–1002.

Galewsky, J., Sobel, A., & Held, I. (2005). Diagnosis of subtropical humidity dynamics using tracers of last saturation. *Journal of the atmospheric sciences*, 62(9), 3353–3367.

Gettelman, A., Seidel, D., Wheeler, M., & Ross, R. (2002). Multidecadal trends in tropical convective available potential energy. *J. Geophys. Res. Atmos.*, 107(D21).

Gill, A. E. (1980). Some simple solutions for heat-induced tropical circulation. *Q. J. Roy. Meteor. Soc.*, 106(449), 447–462.

Giorgi, F., Im, E.-S., Coppola, E., Diffenbaugh, N., Gao, X., Mariotti, L., & Shi, Y. (2011). Higher hydroclimatic intensity with global warming. *Journal of Climate*, 24(20), 5309–5324.

Gregory, J. M., Ingram, W. J., Palmer, M. A., Jones, G. S., Stott, P. A., Thorpe, R. B., Lowe, J. A., Johns, T. C., & Williams, K. D. (2004). A new method for diagnosing radiative forcing and climate sensitivity. *Geophys. Res. Lett.*, 31, L03205.

Gu, G. & Adler, R. F. (2018). Precipitation intensity changes in the tropics from observations and models. *Journal of Climate*, 31(12), 4775–4790.

Hardy, J. & Stolwijk, J. (1966). Partitional calorimetric studies of man during exposures to thermal transients. *Journal of Applied Physiology*, 21(6), 1799–1806.

Hardy, J. D., Du Bois, E. F., & Soderstrom, G. (1938). Basal metabolism, radiation, convection and vaporization at temperatures of 22 to 35 c. *The Journal of Nutrition*, 15(5), 477–497.

He, J., Johnson, N. C., Vecchi, G. A., Kirtman, B., Wittenberg, A. T., & Sturm, S. (2018). Precipitation sensitivity to local variations in tropical sea surface temperature. *Journal of Climate*, 31(22), 9225–9238.

Held, I. M. (2005). The gap between simulation and understanding in climate modeling. *Bulletin of the American Meteorological Society*, 86(11), 1609–1614.

Held, I. M. & Soden, B. J. (2000). Water Vapor Feedback and Global Warming. *Annual Review of Energy and the Environment*, 25, 441–475.

Held, I. M. & Soden, B. J. (2006). Robust Responses of the Hydrological Cycle to Global Warming. *J. Climate*, 19, 5686–5699.

Huang, Y., Ramaswamy, V., & Soden, B. (2007). An investigation of the sensitivity of the clear-sky outgoing longwave radiation to atmospheric temperature and water vapor. *Journal of Geophysical Research: Atmospheres*, 112(D5).

Huffman, G. J., Adler, R. F., Morrissey, M. M., Bolvin, D. T., Curtis, S., Joyce, R., Mc-Gavock, B., & Susskind, J. (2001). Global precipitation at one-degree daily resolution from multisatellite observations. *Journal of hydrometeorology*, 2(1), 36–50.

Huffman, G. J., Bolvin, D. T., Nelkin, E. J., Wolff, D. B., Adler, R. F., Gu, G., Hong, Y., Bowman, K. P., & Stocker, E. F. (2007). The trmm multisatellite precipitation analysis (tmpa): Quasi-global, multiyear, combined-sensor precipitation estimates at fine scales. *Journal of hydrometeorology*, 8(1), 38–55.

Im, E.-S., Pal, J. S., & Eltahir, E. A. (2017). Deadly heat waves projected in the densely populated agricultural regions of south asia. *Science advances*, 3(8), e1603322.

Ingram, W. (2010). A very simple model for the water vapour feedback on climate change. *Quarterly Journal of the Royal Meteorological Society: A journal of the atmospheric sciences, applied meteorology and physical oceanography*, 136(646), 30–40.

ISO (2017). International organization for standardization. ergonomics of the thermal environment – assessment of heat stress using the wbgt (wet bulb globe temperature) index.

Jeevanjee, N., Hassanzadeh, P., Hill, S., & Sheshadri, A. (2017). A perspective on climate model hierarchies. *Journal of Advances in Modeling Earth Systems*, 9(4), 1760–1771.

Johnson, N. C. & Xie, S.-P. (2010). Changes in the sea surface temperature threshold for tropical convection. *Nature Geoscience*, 3(12), 842.

Joshi, M. M., Gregory, J. M., Webb, M. J., Sexton, D. M. H., & Johns, T. C. (2008). Mechanisms for the land/sea warming contrast exhibited by simulations of climate change. *Clim. Dynamics*, 30, 455–465.

Kiladis, G. N., Wheeler, M., Haertel, P., Straub, K., & Roundy, P. (2009). Convectively coupled equatorial waves. *Rev. Geophys.*, 47, RG2003.

Koll, D. D. & Cronin, T. W. (2018). Earth's outgoing longwave radiation linear due to h2o greenhouse effect. *Proceedings of the National Academy of Sciences*, 115(41), 10293–10298.

Kovats, R. S. & Hajat, S. (2008). Heat stress and public health: a critical review. *Annu. Rev. Public Health*, 29, 41–55.

Lindzen, R. & Nigam, S. (1987). On the role of sea surface temperature gradients in forcing low-level winds and convergence in the tropics. *J. Atmos. Sci.*, 44(17), 2418–2436.

Lintner, B. R., Biasutti, M., Diffenbaugh, N. S., Lee, J.-E., Niznik, M. J., & Findell, K. L. (2012). Amplification of wet and dry month occurrence over tropical land regions in response to global warming. *Journal of Geophysical Research: Atmospheres*, 117(D11).

Liu, C. & Allan, R. P. (2013). Observed and simulated precipitation responses in wet and dry regions 1850–2100. *Environmental Research Letters*, 8(3), 034002.

Maher, P., Gerber, E. P., Medeiros, B., Merlis, T. M., Sherwood, S., Sheshadri, A., Sobel, A. H., Vallis, G. K., Voigt, A., & Zurita-Gotor, P. (2019). Model hierarchies for understanding atmospheric circulation. *Reviews of Geophysics*, 57(2), 250–280.

Manabe, S. & Wetherald, R. T. (1975). The effects of doubling the co2 concentration on the climate of a general circulation model. *Journal of the Atmospheric Sciences*, 32(1), 3–15.

Mapes, B. E. (2000). Convective inhibition, subgrid-scale triggering energy, and stratiform instability in a toy tropical wave model. *J. Atmos. Sci.*, 57(10), 1515–1535.

Mitchell, D., Heaviside, C., Vardoulakis, S., Huntingford, C., Masato, G., Guillod, B. P., Frumhoff, P., Bowery, A., Wallom, D., & Allen, M. (2016). Attributing human mortality during extreme heat waves to anthropogenic climate change. *Environmental Research Letters*, 11(7), 074006.

Mora, C., Dousset, B., Caldwell, I. R., Powell, F. E., Geronimo, R. C., Bielecki, C. R., Counsell, C. W., Dietrich, B. S., Johnston, E. T., Louis, L. V., et al. (2017). Global risk of deadly heat. *Nature Climate Change*, 7(7), 501.

Neelin, J., Chou, C., & Su, H. (2003). Tropical drought regions in global warming and el nino teleconnections. *Geophysical Research Letters*, 30(24).

Pal, J. S. & Eltahir, E. A. (2016). Future temperature in southwest asia projected to exceed a threshold for human adaptability. *Nature Climate Change*, 6(2), 197.

Palmen, E. (1948). On the formation and structure of tropical hurricanes. *Geophysica*, 3(1), 26–38.

Pendergrass, A. G. & Gerber, E. P. (2016). The rain is askew: Two idealized models relating vertical velocity and precipitation distributions in a warming world. *Journal of Climate*, 29(18), 6445–6462.

Pfahl, S., O'Gorman, P. A., & Fischer, E. M. (2017). Understanding the regional pattern of projected future changes in extreme precipitation. *Nature Climate Change*, 7(6), 423.

Pierrehumbert, R. (1998). Lateral mixing as a source of subtropical water vapor. *Geophysical research letters*, 25(2), 151–154.

Pierrehumbert, R. T. & Roca, R. (1998). Evidence for control of atlantic subtropical humidity by large scale advection. *Geophysical Research Letters*, 25(24), 4537–4540.

Polson, D. & Hegerl, G. (2017). Strengthening contrast between precipitation in tropical wet and dry regions. *Geophysical Research Letters*, 44(1), 365–373.

Polson, D., Hegerl, G., Allan, R., & Sarojini, B. B. (2013). Have greenhouse gases intensified the contrast between wet and dry regions? *Geophysical Research Letters*, 40(17), 4783–4787.

Raghuraman, S. P., Paynter, D., & Ramaswamy, V. (2019). Quantifying the drivers of the clear sky greenhouse effect, 2000–2016. *Journal of Geophysical Research: Atmospheres*, 124(21), 11354–11371.

Rajah, K., O'Leary, T., Turner, A., Petrakis, G., Leonard, M., & Westra, S. (2014). Changes to the temporal distribution of daily precipitation. *Geophysical Research Letters*, 41(24), 8887–8894.

Raval, A., Oort, A., & Ramaswamy, V. (1994). Observed dependence of outgoing longwave radiation on sea surface temperature and moisture. *Journal of climate*, 7(5), 807–821.

Raval, A. & Ramanathan, V. (1989). Observational determination of the greenhouse effect. *Nature*, 342(6251), 758–761.

Raymond, D. & Zeng, X. (2005). Modelling tropical atmospheric convection in the context of the weak temperature gradient approximation. *Q.J. Roy. Meteorol. Soc.*, 131(608), 1301–1320.

Raymond, D. J. (1995). Regulation of moist convection over the west pacific warm pool. *J. Atmos. Sci.*, 52(22), 3945–3959.

Rayner, N., Parker, D. E., Horton, E., Folland, C. K., Alexander, L. V., Rowell, D., Kent, E., & Kaplan, A. (2003). Global analyses of sea surface temperature, sea ice, and night marine air temperature since the late nineteenth century. *Journal of Geophysical Research: Atmospheres*, 108(D14).

Reynolds, R. W., Smith, T. M., Liu, C., Chelton, D. B., Casey, K. S., & Schlax, M. G. (2007). Daily high-resolution-blended analyses for sea surface temperature. *Journal of Climate*, 20(22), 5473–5496.

Romps, D. M. (2014). An analytical model for tropical relative humidity. *Journal of Climate*, 27(19), 7432–7449.

Santer, B. D., Mears, C., Wentz, F., Taylor, K., Gleckler, P., Wigley, T., Barnett, T., Boyle, J., Brüggemann, W., Gillett, N., et al. (2007). Identification of human-induced changes in atmospheric moisture content. *Proceedings of the National Academy of Sciences*, 104(39), 15248–15253.

Sherwood, S. C. (2018). How important is humidity in heat stress? *Journal of Geophysical Research: Atmospheres*, 123(21), 11–808.

Sherwood, S. C. & Huber, M. (2010). An adaptability limit to climate change due to heat stress. *Proceedings of the National Academy of Sciences*, 107(21), 9552–9555.

Sherwood, S. C. & Meyer, C. (2006). The General Circulation and Robust Relative Humidity. *J. Climate*, 19, 6278–6279.

Shine, K. P. & Sinha, A. (1991). Sensitivity of the earth's climate to height-dependent changes in the water vapour mixing ratio. *Nature*, 354(6352), 382–384.

Sobel, A., Held, I., & Bretherton, C. (2002). The ENSO Signal in Tropical Tropospheric Temperature. *J. Climate*, 15(18), 2702–2706.

Sobel, A. H. & Bretherton, C. S. (2000). Modeling tropical precipitation in a single column. *J. Climate*, 13(24), 4378–4392.

Sobel, A. H., Nilsson, J., & Polvani, L. M. (2001). The weak temperature gradient approximation and balanced tropical moisture waves. *J. Atmos. Sci.*, 58(23), 3650–3665.

Soden, B. & Held, I. (2006). An Assessment of Climate Feedbacks in Coupled Ocean-Atmosphere Models. *J. Climate*, 19(2003), 3354–3360.

Soden, B. J., Held, I. M., Colman, R., Shell, K. M., Kiehl, J. T., & Shields, C. A. (2008). Quantifying climate feedbacks using radiative kernels. *Journal of Climate*, 21(14), 3504–3520.

Stephens, G. L. & Greenwald, T. J. (1991). The earth's radiation budget and its relation to atmospheric hydrology: 2. observations of cloud effects. *Journal of Geophysical Research: Atmospheres*, 96(D8), 15325–15340.

Stephens, G. L., Kahn, B. H., & Richardson, M. (2016). The super greenhouse effect in a changing climate. *Journal of Climate*, 29(15), 5469–5482.

Taylor, K. E., Stouffer, R. J., & Meehl, G. A. (2012). An overview of cmip5 and the experiment design. *Bull. Am. Meteorol. Soc.*, 93(4), 485–498.

Valero, F. P., Collins, W. D., Pilewskie, P., Bucholtz, A., & Flatau, P. J. (1997). Direct radiometric observations of the water vapor greenhouse effect over the equatorial pacific ocean. *Science*, 275(5307), 1773–1776.

Vogel, M. M., Orth, R., Cheruy, F., Hagemann, S., Lorenz, R., van den Hurk, B. J., & Seneviratne, S. I. (2017). Regional amplification of projected changes in extreme temperatures strongly controlled by soil moisture-temperature feedbacks. *Geophysical Research Letters*, 44(3), 1511–1519.

Waliser, D. E. & Graham, N. E. (1993). Convective cloud systems and warm-pool sea surface temperatures: Coupled interactions and self-regulation. *Journal of Geophysical Research: Atmospheres*, 98(D7), 12881–12893.

Willett, K. M., Gillett, N. P., Jones, P. D., & Thorne, P. W. (2007). Attribution of observed surface humidity changes to human influence. *Nature*, 449(7163), 710.

Willett, K. M. & Sherwood, S. (2012). Exceedance of heat index thresholds for 15 regions under a warming climate using the wet-bulb globe temperature. *International Journal of Climatology*, 32(2), 161–177.

Williams, E. & Renno, N. (1993). An analysis of the conditional instability of the tropical atmosphere. *Monthly Weather Review*, 121(1), 21–36.

Williams, I. N. & Pierrehumbert, R. T. (2017). Observational evidence against strongly stabilizing tropical cloud feedbacks. *Geophysical Research Letters*, 44(3), 1503–1510.

Williams, I. N., Pierrehumbert, R. T., & Huber, M. (2009). Global warming, convective threshold and false thermostats. *Geophysical Research Letters*, 36(21).

Zhang, C. (1993). Large-scale variability of atmospheric deep convection in relation to sea surface temperature in the tropics. *Journal of Climate*, 6(10), 1898–1913.

Zhang, G. J. & Mcphaden, M. J. (1995). The relationship between sea surface temperature and latent heat flux in the equatorial pacific. *Journal of climate*, 8(3), 589–605.

Zhang, Y. & Fueglistaler, S. (2019). Mechanism for increasing tropical rainfall unevenness with global warming. *Geophysical Research Letters*, 46(24).

Zhang, Y. & Fueglistaler, S. (2020). How tropical convection couples high moist static energy over land and ocean. *Geophysical Research Letters*, 47(2), e2019GL086387.

Zhang, Y., Held, I., & Fueglistaler, S. (2021). Projections of tropical heat stress constrained by atmospheric dynamics. *Nature Geoscience*, 14, 133–137.

Zhang, Y., Jeevanjee, N., & Fueglistaler, S. (2020). Linearity of outgoing longwave radiation: From an atmospheric column to global climate models. *Geophysical Research Letters*, Under review, DOI:10.1002/essoar.10503351.1.